Science of the Total Environment 798 (2021) 149241

Contents lists available at ScienceDirect

Science of the Total Environment

journal homepage: www.elsevier.com/locate/scitotenv

Oceanography time series reveals annual asynchrony input between oceanic and estuarine waters in Patagonian fjords

Iván Pérez-Santos [a,b,c,*], Patricio A. Díaz [a,d], Nelson Silva [e], René Garreaud [f], Paulina Montero [c,b], Carlos Henríquez-Castillo [g,h], Facundo Barrera [f,i], Pamela Linford [j], Constanza Amaya [k], Sergio Contreras [i], Claudia Aracena [l,m], Elías Pinilla [n], Robinson Altamirano [a,d], Luis Vallejos [a,d], Javiera Pavez [c], Juan Maulen [a]

[a] Centro i-mar de la Universidad de los Lagos, Puerto Montt, Chile
[b] Centro de Investigación Oceanográfica COPAS Sur-Austral, Universidad de Concepción, Chile
[c] Centro de Investigaciones en Ecosistemas de la Patagonia (CIEP), Coyhaique, Chile
[d] CeBiB, Universidad de Los Lagos, Puerto Montt, Chile
[e] Pontificia Universidad Católica de Valparaíso, Chile
[f] Centro de Ciencia del Clima y la Resilencia (CR2), Universidad de Chile, Chile
[g] Laboratorio de Fisiología y Genética Marina, Centro de Estudios Avanzados en Zonas Áridas (CEAZA), Coquimbo, Chile
[h] Facultad de Ciencias del Mar, Universidad Católica del Norte, Coquimbo, Chile
[i] Facultad de Ciencias & Centro de Investigación en Biodiversidad y Ambientes Sustentables (CIBAS), Universidad Católica de la Santísima Concepción, Concepción, Chile
[j] Programa de Doctorado en Ciencias mención Conservación y Manejo de Recursos Naturales, Centro i-mar, Universidad de Los Lagos, Puerto Montt, Chile
[k] Departamento de Geofísica, Universidad de Concepción, Chile
[l] Laboratorio Costero de Recursos Acuáticos de Calfuco, Universidad Austral de Chile, Valdivia, Chile
[m] Centro de Investigación en Recursos Naturales y Sustentabilidad, Universidad Bernardo O'Higgins, Avenida Viel 1497, Santiago, Chile
[n] Instituto de Fomento Pesquero (IFOP), CTPA-Putemún, Castro, Chile

HIGHLIGHTS

- An asynchronous input of oceanic and estuarine waters was found at northern Patagonia.
- Surface salinity variability responds to the phase of the Indian Ocean Dipole.
- Biogeochemistry at the surface layer was synchronic with the salinity variation.
- A shift in phytoplankton composition from late winter to summer was observed.
- No biogeochemical signs of eutrophication were found at the Reloncaví sound.

GRAPHICAL ABSTRACT

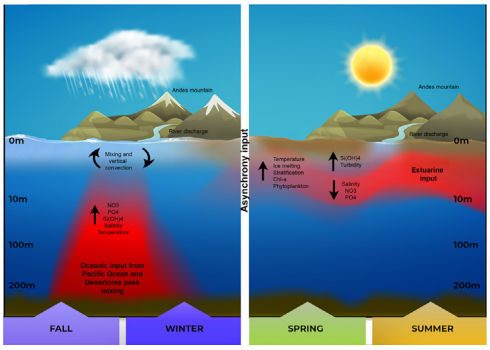

ARTICLE INFO

Article history:
Received 28 May 2021
Received in revised form 20 July 2021
Accepted 20 July 2021
Available online 27 July 2021

Editor: Fernando A.L. Pacheco

ABSTRACT

The postglacial Patagonian fjord system along the west coast of southern South America is one of the largest stretches of the southern hemisphere (SH) fjord belt, influenced by the SH westerly wind belt and continental freshwater input. This study reports a 3-year monthly time series (2017–2020) of physical and biogeochemical parameters obtained from the Reloncaví Marine Observatory (OMARE, Spanish acronym) at the northernmost embayment and fjord system of Patagonia. The main objective of this work was to understand the land–atmosphere–ocean interactions and to identify the mechanisms that modulate the density of phytoplankton. A key finding of this study was the seasonally varying asynchronous input of oceanic and estuarine water. Surface lower salinity and warmer estuarine water arrived in late winter to summer, contributing to water column

* Corresponding author at: Centro i-mar de la Universidad de los Lagos, Puerto Montt, Chile.
E-mail address: ivan.perez@ulagos.cl (I. Pérez-Santos).

https://doi.org/10.1016/j.scitotenv.2021.149241
0048-9697/

Keywords:
Oceanography
Patagonian fjords
Biogeochemistry
Atmospheric mode
Time series
Marine observatory

stability, followed by subsurface higher salinity and less warmer oceanic water during fall–winter. In late winter 2019, an interannual change above the picnocline due to the record-high polarity of the Indian Ocean Dipole inhibited water column stability. The biogeochemical parameters (NO_3^-, NO_2^-, PO_4^{3-}, $Si(OH)_4$, pH, and dissolved oxygen) responded to the surface annual salinity variations, and oceanic water mass contributed greatly to the subsurface inorganic nutrient input. The water column N/P ratio indicated that no eutrophication occurred, even under intense aquaculture activity, likely because of the high ventilation dynamics of the Reloncaví Sound. Finally, a shift in phytoplankton composition, characterized by surface chlorophyll-a maxima in late winter and deepening of spring–summer blooms related to the physicochemical conditions of the water column, was observed. Our results support the ecosystem services provided by local oceanography processes in the north Patagonian fjords. Here, the anthropogenic impact caused by economic activities could be, in part, chemically reduced by the annual ventilation cycle mediated by the exchange of oceanic water masses into Patagonian fjords.

Nomenclature

SH	Southern hemisphere
OMARE	Spanish acronym for Observatorio Marino Reloncaví
IPCC	Intergovernmental panel on climate change
WWB	Westerly wind belt
SPSA	Southeast Pacific subtropical anticyclone
ENSO	El Niño-Southern oscillation
SAM	Southern annular mode
SAAW	Subantartic water mass
WOA	Word Ocean Atlas
ESSW	Equatorial subsurface water
AAIW	Antartic intermediate water
PCUC	Peru-Chile undercurrent
ACC	Antartic circumpolar water
MSAAW	Modified subantartic water
EW	Estuarine water
CTD	Conductivity temperature and depth
DO	Dissolved oxygen
SLP	Sea level pressure
NCEP	National Center for Environmental Prediction
NCAR	National Center for Atmospheric Research
SEF	Salt effect factor
CIMAR	Program of Marine Scientific Research Cruise in Remote Areas (Spanish acronyms)
Si*	Silica star
Chl a	Chlorophyll-*a*
N^2	Brunt–Väisälä frequency
n_s	stratification parameter
Kf	Brackish water layer
PEA	Potential energy anomaly
S_A	Absolute salinity
AOU	apparent oxygen utilization
PP	Primary production

1. Introduction

Freshwater supply from continental basins to oceans around the world generates estuarine systems. Fjords are the deepest (300–400 m) estuaries and are distributed in mid-high latitudes, mainly poleward at 40° latitude (Valle-Levinson, 2010). Similar to many aquatic ecosystems, Patagonian fjords in South America face substantial environmental and anthropogenic pressures (Iriarte et al., 2010; Iriarte, 2018) due to climate change and hydrographic variability. For example, recent reductions in global precipitation have resulted in the diminishing of freshwater supply (IPCC, 2013, 2014; Sauter, 2020), altering the gravitational circulation, stratification regime, and biogeochemical cycles of the oceans (Bianchi et al., 2020). In contrast, an SST increase has intensified glacial freshwater drainage, enhancing sea-level rise in Patagonian fjords in recent decades (Rignot et al., 2003). In this context, ecosystems have become more vulnerable. Therefore, it is necessary to seek new adaptation measures (Nazarnia et al., 2020) to mitigate the effects of sea level rise due to climate change. Furthermore, intense aquaculture activity and the continuous increase in human settlements along the Patagonian fjord coastlines have resulted in large amounts of organic matter being added to the water of the fjords (Quiñones et al., 2019), contributing to the degradation of their aquatic environments (Andersen et al., 2006). As estuarine ecosystems, these fjords are influenced by the land, ocean, and atmosphere, providing opportunities for comprehensive interdisciplinary studies to understand the interactions between coastal oceanography processes, atmospheric circulation, and biogeochemical cycle responses.

In general, coastal oceanographic studies of fjords focus on the tidal regimen and hydrographic conditions as two important drivers'of fjord circulation (Farmer and Freeland, 1983; Inall and Gillibrand, 2010). In the Patagonian fjords, a reduction in surface salinity occurs due to freshwater input from melting ice, river runoff, and precipitation (Dávila et al., 2002), which results in a horizontal salinity gradient that contributes to the formation of the estuarine or gravitational circulation (Valle-Levinson, 2010), where the surface current moves seaward, and a deeper current moves landward (Hansen and Rattray, 1965). In addition, winds play an important role in the residual circulation (moving water in periods of days), transporting surface waters along the fjord, and thus causing an increase in the estuarine circulation (Becherer et al., 2016). Therefore, tidal, salinity, and wind data are necessary variables that should be incorporated into fjord oceanography studies (Burchard et al., 2011; Castillo et al., 2012; Valle-Levinson et al., 2007, 2014).The interactions between oceanic water masses and estuarine water bodies can produce asynchronous processes among the vertical layers in deep estuaries, such as fjord systems (LeBlond et al., 1991; Masson, 2002; Pawlowicz, 2017). In the Salish Sea, located in the British Columbia fjord system of Canada, colder/warmer waters were observed in summer/winter down the 200 m profile. This paradoxical situation is explained by atmospheric forcing (Pawlowicz, 2001). In this fjord system, a portion of the surface water which is heated during the boreal summer is transported to the adjacent oceanic water, and the other portion of warmer water is mixed in fjord areas where intense vertical mixing occurs, staying in intermediate and deep layers of fjords (LeBlond et al., 1991; Masson, 2002; Pawlowicz, 2017).

The Patagonian fjords extend over ~240,000 km^2 from 41°S to 56°S along the coastline of southern Chile, thus receiving the influence of the vast South Pacific Ocean. This fjord system is connected to rivers that originate in the austral Andes mountains, less than 100 km from the ocean. This region exhibits a temperate, hyper-humid climate with mean precipitation between 2000 and 5000 mm/year, caused by the frequent passage of extra tropical storms (Garreaud, 2009; Pérez-Santos et al., 2019) embedded in the southern hemisphere (SH) westerly wind belt (WWB) impinging against the austral Andes year-round (Fig. 1a). During austral summer (December–February), however, the Southeast Pacific Subtropical Anticyclone (SPSA) expands southward, reaching the northern part of western Patagonia, thus

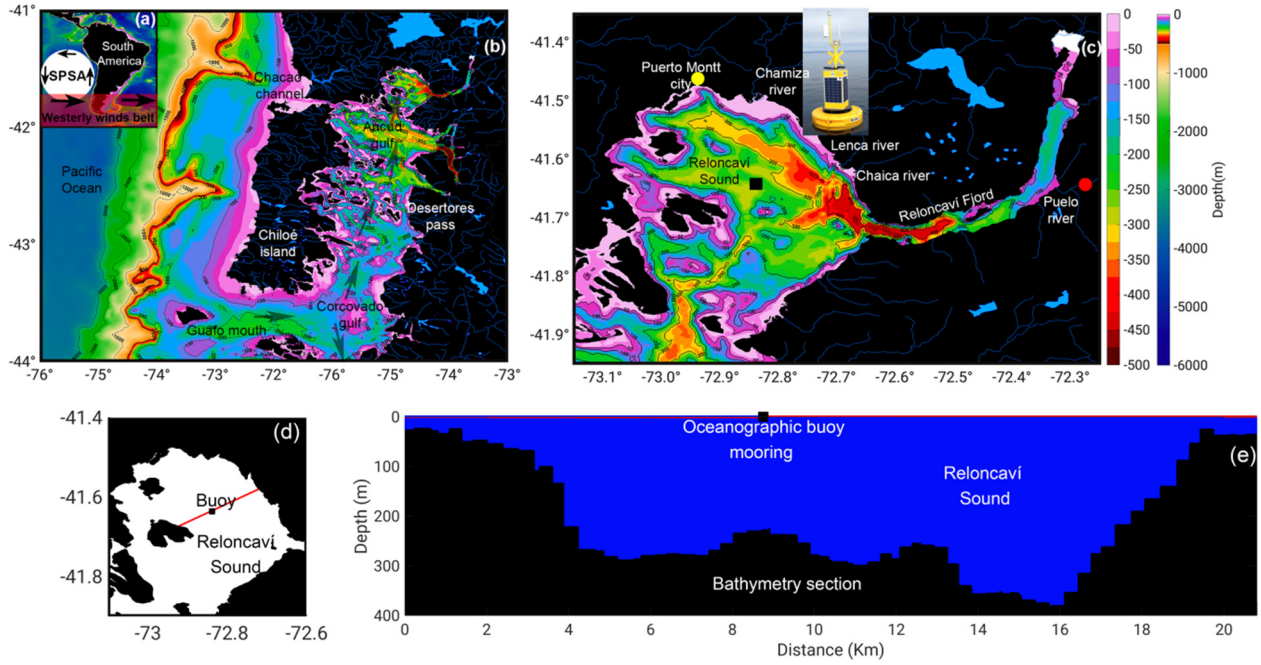

Fig. 1. (a) Schematic of the atmospheric circulation in South America, and the South Westerly Winds (SWW) belt, and the Southeast Pacific Subtropical Anticyclone (SPSA). (b) Map of North Patagonia where Reloncaví Sound connects with the Pacific Ocean through the Chacao Channel, and to the Inner Sea of Chiloé though the Ancud, and Corcovado Gulfs. (c) Location of the oceanographic-meteorological OMARE observatory (black square), the historical meteorological (DGAC), and precipitation (DGA) stations (red dot).The bathymetry of the Reloncaví fjord system (color scale indicates depth in m) allows the entrance and distribution of subsurface oceanic water from adjacent Pacific Ocean. (d) Cross section (red line) used to show the (e) bathymetry features of Reloncaví Sound with the oceanographic-meteorological buoy mooring.

causing a reduction in precipitation and an increase in air temperature. The intensity and position of the SPSA and the south westerly wind SWW can be modified by several planetary-scale atmospheric modes (e.g., Garreaud, 2009) at interannual and longer timescales, including the El Niño Southern Oscillation (ENSO) and the Southern Annular Mode (SAM), and, more recently, by human-driven climate change. In fact, a recent southward displacement of the SPSA has been reported (Narváez et al., 2019; Pérez-Santos et al., 2019), extending poleward the influence of upwelling conditions up to ~43° S.

In general, estuarine systems are biologically productive and have high levels of primary production (Burrell, 1988). The continuous increase in nutrient supply due to anthropogenic activities (e.g., agriculture and aquaculture) contributes to enhanced primary production, thus changing the trophic status to more eutrophic conditions in many estuaries around the world (Aitkenhead and McDowell, 2000; Andersen et al., 2006; Carstensen et al., 2013). A review of several definitions of eutrophication carried out by Andersen et al. (2006) suggests that the most suitable definition of coastal eutrophication is "the enrichment of water by nutrients, especially nitrogen and/or phosphorus and organic matter, causing an increased growth of algae, and higher forms of plant life to produce an unacceptable deviation in structure, function, and stability of organisms present in the water, and to the quality of water concerned, compared to reference conditions". Patagonian fjords are continuously exchanged with the adjacent oceanic-rich water, a process which transports large concentrations of nitrate (20–30 μM) and phosphate (2–3 μM), and silicic acid (15–25 μM) into the fjords (Silva et al., 2009). Additionally, high concentrations of Nitrate (10–20 μM), phosphate (0.5–2 μM), andsilicic acid (20–100 μM) (González et al., 2019) arrive every spring-summer to the fjords due to continental freshwater discharge (Aracena et al., 2011; Silva and Vargas, 2014; Torres et al., 2014). Therefore, high nutrient concentrations and light availability, especially in the Inner Sea of Chiloe and Northern Patagonia, favor high primary production rates (4.8– 9.4 g C m^{-3} d^{-1}) during summer seasons (Aracena et al., 2011; Montero et al., 2011; Daneri et al., 2012; González et al., 2013).

This study aims to depict the relationship between oceanic and estuarine water inputs into the Reloncaví Sound, the regional hydrographic and climate regimes, response of the biogeochemistry, and phytoplankton biomass in the water column. To conduct our research, we coupled the data recorded from an atmospheric and oceanographic buoy with long-term climate data, and a monthly sampling program from the Reloncaví Marine Observatory (OMARE, Spanish acronym) to understand the natural variability and the associated anthropogenic influence on the Reloncaví Sound and its surrounding areas between 2017 and 2020. Hydrographic and biogeochemical data collected over this period showed asynchrony between the surface estuarine and subsurface oceanic water masses, which was the motivation behind conducting this research. One of the relevant questions addressed is how atmospheric and oceanographic conditions impact such asynchrony, and how the water column responds to this phenomenon. In a broader context, the OMARE program is oriented towards understanding modern oceanography dynamics in this ecosystem exposed to intense anthropogenic activity, likely allowing for efficient functioning due to the annual cycle of ventilation from the entrance of oceanic rich-nutrient subantarctic surface water (SAAW) towards the inner Patagonian fjord system.

The results and discussion of this investigation are presented in sections. Section 3 describes the results of the annual and interannual cycles of hydrographical and biogeochemical parameters (nitrogen, phosphate, and silicic acid). These results allowed for the first report of the asynchrony input of water masses in the Southern Hemispheric fjord belt. This section also includes a detailed description of the water column biogeochemical response to such variability and phytoplankton distribution and density, emphasizing late winter and summer phytoplankton blooms. In Section 4, we discuss the surface and subsurface water column processes that influence asynchrony. We further addressed the oceanographic and climatic processes that enhance such asynchrony, and discuss how they influence the hydrographic-biogeochemical cycles in the Reloncaví sound. Additionally, this section highlights climatic anomalies such as the Indian Ocean Dipole Mode (IOD) altering the freshwater supply into the Reloncaví sound during

2019 and its effects on the temporal and spatial distribution of phytoplankton assemblages during the entire study period. Finally, our discussion focuses on the asynchrony mechanism of oceanic water input and its effects on the biogeochemistry of this ecosystem.

2. Materials and methods

2.1. Study area

The Reloncaví Sound (41°40′S; 74°45′W) is an embayment of the Inner Sea of Chiloé, and it slightly overlaps with the southern part of the Lakes District of southern Chile. This fjord system has undergone a recent geological evolution from a glacial origin, followed by a glacio-fluvial/glacio-lacustrine phase, and ending in the present marine fjord ecosystem. High-resolution reflection seismic data has revealed a complex depositional system in which the Reloncaví fjord is divided into four principal basins following a depth gradient towards the sound. The convergence between the Reloncaví fjord and the Reloncaví sound is located in the deepest zone at 458 m (Fig. 1c). The sound depth distribution is characterized by a deep channel system with two main branches exceeding 350 m in depth (Aracena, 2005). The presence of islands of different sizes in the embayment contributes to heterogeneity in terms of geomorphology and depth distribution. This region is directly influenced by oceanic waters from the adjacent Pacific Ocean (Pérez-Santos et al., 2014; Saldías et al., 2019; Strub et al., 2019) through the Chacao Channel and Corcovado Gulf, but is also affected by estuarine inputs (Sievers and Silva, 2008) and continental waters (Calvete and Sobarzo, 2011). The entire area is considered a world heritage site, and hosts one of the last pristine ecosystems on Earth, providing several ecosystem services for the Earth. The sound coastline is home to more than 200,000 inhabitants, largely concentrated in the city of Puerto Montt, whose main activities are aquaculture (salmon farming and mussel culture), agriculture, cattle raising, fisheries, and tourism. All these activities are responsible for the release of large amounts of organic matter (Quiñones et al., 2019).

2.1.1. Coastal oceanography

Oceanographic conditions in the water adjacent to the Chilean continental margin between 31°S and 47°S were described using hydrographic and chemical data from the World Ocean Atlas (WOA) 2018, (Boyer et al., 2018) (Fig. S1). This area is characterized by the presence of three water masses: (1) the SAAW (11.5 °C and 33.8 g kg^{-1}), (2) Equatorial Subsurface Water (ESSW; 12.5 °C and 34.9 gkg^{-1}), and (3) Antarctic Intermediate Water (AAIW; 3.0 °C and 34.0 g kg^{-1}) (Silva et al., 2009). The ESSW is characterized by a salinity of 34.9 g kg^{-1}, high concentrations of nitrate (20–32 μM), phosphate (2.2–2.8 μM), and silicic acid (15–25 μM), and a minimum of dissolved oxygen (DO) between 2 and 3 mL L^{-1} (Silva et al., 2009). This ESSW water mass is transported poleward by the Peru Chile Undercurrent (PCUC) (Leth et al., 2004) and flows parallel to the Peru-Chile coastline to~48°S (Hormazábal et al., 2006; Neshyba et al., 1989; Penven et al., 2005).

The SAAW is part of the surface Antarctic Circumpolar Water (ACC) (Emery, 2001) and has been observed to reach as high as~35°S (Hernández-Vaca et al., 2017). Close to the Patagonian fjord coastline, the SAAW receives a freshwater supply from Patagonian rivers, and glacial ice melting, reducing the salinity to 33.0–33.9 gkg^{-1} (Dávila et al., 2002; Saldías et al., 2019). Both the oceanic SAAW and ESSW off Chiloé flow into the northern Patagonian channels, mainly through the Guafo Mouth (~200 m deep) and towards the Corcovado Gulf. Subsequently, such water masses move northward through the Corcovado Gulf, Ancud Gulf, and Reloncaví Sound (Castillo et al., 2016; Pérez-Santos et al., 2014; Silva and Vargas, 2014). Once SAAW is inside this fjord system, it is mixed with continental (Salinity = 0–2 gkg^{-1}) and estuarine (Salinity = 2–31 gkg^{-1}) waters (EW), forming the modified Subantarctic water (MSAAW) with a salinity range of31.0–33.0 gkg^{-1} (Sievers and Silva, 2008).

2.1.2. Climate

Puerto Montt, the capital of Los Lagos region, is on the N — E coast of the Reloncaví Sound. The mean air temperature ranges from ~6 °C in July (austral winter) to ~15 °C in January (summer). Mid-latitude depressions embedded in the WWB cause high precipitation (average 2000–3000 mm/year) along the coast, which can be enhanced up to ~5000 mm/year inland due to the orographic uplift of the Austral Andes (Viale and Garreaud, 2015). Many storms which reach western Patagonia feature atmospheric rivers, long filaments of high moisture transport (Viale et al., 2018), whose interaction with the Andes results in intense precipitation events (>100 mm/day) and freshwater drainage (Valenzuela and Garreaud, 2019).

At interannual timescales, persistent pressure anomalies over the southern tip of South America can alter the WWB at midlatitudes and, subsequently, the precipitation pattern over western Patagonia. Climate variability has been linked to the ENSO and the SAM (Garreaud, 2018). The major impact of the ENSO manifests during austral summer: under "El Niño" ("La Niña") conditions thereis a tendency for high (low) pressure anomalies and precipitation deficit (excess) in north Patagonia (Montecinos and Aceituno, 2003). SAM arises from the eddy-mean flow interaction of the high-latitude atmospheric circulation and fluctuates between its positive and negative phases at monthly or longer time scales. During its positive phase, there are negative pressure anomalies south of 55°S, and positive anomalies at midlatitudes causing drier conditions in northern Patagonia (Gillett et al., 2006). In contrast, the negative phase of the SAM brings more precipitation to this region. SAM has also exhibited a significant trend towards its positive polarity during austral summer/fall over the last 3–4 decades, which is attributed to stratospheric ozone (O_3) depletion and the increase in the concentration of atmospheric greenhouse gases. The SAM tendency towards positive polarity has driven a drying trend since the mid-1970s across Patagonia (Boisier et al., 2019) and climate models predict this drying trend to continue for the remainder of the 21st century (Aguayo et al., 2019).

2.2. Atmospheric and oceanographic buoy

The atmospheric and oceanographic records used in the study were obtained from a METOCEAN buoy manufactured by OSIL, Environmental Instruments, and Systems (https://osil.com/). The buoy has a diameter of 1.9 m and is anchored in the central area of the Reloncaví Sound (41° 38′.183 S, 72° 50′.069 W) at a depth of ~240 m (Fig. 1b). The METOCEAN buoy was equipped with a meteorological station (Gill GMX500, sensors for air temperature, atmospheric pressure, and wind), and a conductivity, temperature, depth instrument (CTD) and an AML Metrec-XL (Table 1). Additionally, the CTD was equipped with sensors for dissolved oxygen (DO), pH, and fluorescence (Aanderaa Oxygen optode, Idronaut pH, and Turner Cyclops-7, respectively). The CTD instrument was installed at a depth of 1.5 m, and captured data were recorded with an hourly temporal resolution. The temperature and salinity data from the CTD were converted to conservative temperature (Θ, in °C) and absolute salinity (S_A, in g kg^{-1}), according to the thermodynamic equation of Seawater 2010 (Ioc, S., IAPSO, 2010). Data collection started on the 16th of March 2017, and has been continuously operating since that date. The buoy data are free access and available online at http://cdom.cl and http://goa-on.org.

2.3. Long-term climate data

Daily mean rainfall data were obtained from a meteorological weather station provided by the Chilean Weather Service (DMC) at Puerto Montt (41.46°S/72.93°W, yellow circle in Fig. 1c). Stream flow data were provided by the Dirección General de Aguas (DGA) from

the record at station Carrera Basilio (41.6°S/72.2°W; red circle in Fig. 1c) located close to the mouth of Puelo River in the Reloncaví Fjord an area 8500 km^2. Large-scale atmospheric circulation was characterized using monthly means of sea level pressure (SLP)and geopotential height at selected pressure levels obtained from the National Center for Environmental Prediction (NCEP) and the National Center for Atmospheric Research (NCAR) reanalysis, available from 1948 onwards on a 2.5° × 2.5° latitude–longitude grid (details in Kalnay et al., 1996). Monthly indices of ENSO, SAM, and the Indian Ocean Dipole (IOD) were obtained from the repository maintained by the NOAA Physical Sciences Laboratory (PSL) available online at https://www.psl.noaa.gov/data/climateindices.

2.4. Monthly sampling program

In tandem with the deployment of the buoy, the OMARE observatory began a monthly monitoring program in March 2017, aiming at understanding the natural variability and the associated anthropogenic influence on the Reloncaví Sound and surrounding areas. A second CTD with identical technical characteristics (AML Metrec-XL) was used fora monthly time series of physical (temperature and salinity) and chemical parameters (DO and pH) at the position of the buoy. The time series covered the period from March 2017 to March 2020, capturing CTD data from the surface layer to ~220 m depth with a vertical sampling rate of 24 Hz. Additionally, a Niskin bottle (5 L) was used to collect samples at standard depths (0, 5, 10, 15, 25, 50, 75, 100, 125, 150, and 200 m) for inorganic nutrients (NO_3^-, NO_2^-, PO_4^{3-}, and $Si(OH)_4$), pH, chlorophyll-*a*, phytoplankton density, and composition. Samples were filtered through a 0.7 μm filter using a peristaltic pump and stored at −20 °C in 50 mL acid-cleaned high-density polyethylene bottles. These samples were analyzed with a nutrient auto-analyzer (Technicon) according to the methods proposed by Atlas et al. (1971). Only nitrite was measured using spectrophotometry (Strickland and Parsons, 1972). The silicic acid results were corrected by the salt effect factor (SEF) and presented as Si.SEF (Eq. (1)). Two types of sensors and methods were used for the pH measurement. From March 2017 to January 2020, pH was measured using a glass sensor (Hidronaut) attached to the CTD-O equipment. The pH was also measured in collected water samples at standard depths using the Phyter sensor, which is based on spectrophotometry. This portable equipment has a detection limit of ~0.01, and a pH range between 7.4– 9.0. Additionally, historical inorganic nutrient data obtained from the Program of Marine Scientific Research Cruise in Remote Areas (CIMAR, Spanish acronyms) in the Reloncaví fjord and sound were used. These oceanographic cruises were conducted in 1995 (CIMAR-1), 2004 (CIMAR-10), 2005 (CIMAR-11), 2006 (CIMAR-12), 2011 (CIMAR-17), and 2013 (CIMAR-19).

Arjonilla and Blasco (2003) reported that salinity affects silicic acid concentrations, but not nitrite and phosphate concentrations. The salinity effect was considered due to the wide variation range (20– 33 gkg^{-1}) in this estuarine ecosystem. Therefore, we calculated the salt effect factor (SEF) as

$$SEF = 1.3 - 8.253 \times 10^{-3} S \quad (1)$$

where S is the in situ salinity. To estimate the real concentration of silicic acid, Eq. (2) was used:

$$[Si(OH)_4]_{real} = \frac{[Si(OH)_4]_{measured}}{SEF} \quad (2)$$

Using the concentration values of nitrate and corrected silicic acid (Si.SEF), silica star (Si*) was calculated as the molar difference between $[Si(OH)_4]$ and $[(NO_3^-)]$ (Torres et al., 2014). Positive Si* values favor diatom growth over other dominant phytoplankton groups, while negative Si* values suggest that other phytoplankton groups could dominate.

Water samples for chlorophyll-*a* (Chl-a) were filtered through 25 mm 0.7 μm GF/F filters and immediately frozen at −80 °C. Extractions were performed in 10 mL of acetone 90% for 24 h at 4 °C in the dark. Chl-a was measured by fluorometry in a Turner Designs Trilogy Laboratory Fluorometer (Holm-Hansen et al., 1965).

For analyses of phytoplankton density, water samples were collected from six discrete depths (from surface to 50 m depth) using a 5 L Niskin bottle. Samples were stored in 120 mL clear plastic bottles and preserved in 1% Lugol iodine solution (alkaline). From each sample, a 10 mL subsample was placed in a sedimentation chamber and allowed to settle for 12 h (Utermöhl, 1958) prior to identification at 40× and 100× under an inverted microscope (Carl Zeiss, Axio Observer A.1). Finally, taxonomic descriptions from Tomas (1997) were used to identify phytoplankton.

2.5. Derived parameters and statistical approach

The monthly time series of temperature and salinity profiles were used to quantify the stratification and mixing conditions of the water column throughout several indexes (Fig. 4), including the Brunt–Väisälä frequency (N^2) (Stewart, 2002), the stratification parameter (n_s) (Haralambidou et al., 2010), the surface brackish water layer (*Kf*) (Blanton and Atkinson, 1983), and the potential energy anomaly (PEA, ϕ) (Simpson et al., 1979).

The N^2 was calculated using the following formula:

$$N^2 = -gE \quad (3)$$

where*g* is the acceleration due to gravity, and *E* is the static stability of the water column, defined as

$$E = -\frac{1}{\rho}\frac{\delta\rho}{\delta z} \quad (4)$$

where ρ is the water density (1025 kgm^{-3}) and *z* is the depth. The *E* values were classified as follows: E > 0, stable water column; E = 0, neutral stability of water column; and E < 0, unstable water column (Stewart, 2002).

For calculating n_s, the following formula applied was used:

$$n_s = \frac{S_{20m} - S_{1m}}{0.5(S_{20m} + S_{1m})} \quad (5)$$

where*S* is the salinity value at 20 m (S_{20m}) and at the surface layer (S_{1m}). ns > 1, 0.1 < ns < 1, and ns < 0.1 correspond to a highly stratified, partially mixed, and fully mixed water column, respectively (Haralambidou et al., 2010).

On the other hand, the *Kf* equation used was

$$K_f = \int_{-D} \frac{(S_{ref} - S_{(z)})}{(S_{ref})} dz \quad (6)$$

Table 1
Oceanographic-meteorological instruments and sensors installed at the oceanographic buoy in Reloncaví Sound.

Equipment	Sensors	Range	Accuracy (+/−)
CTD AML Metrec-XL	Pressure	0–500 dbar	0.05%
	Temperature	−2° a 32 °C	0.005 °C
	Conductivity	0–90 mS/cm	±0.01 mS/cm
	Dissolved oxygen	0–800 μM	5%
	Fluorescence	0–5 Voltage	0.0004
	Turbidity	0–3000 NTU	2%
	pH	0–14	0.01
Gill GMX500	Wind speed	0.01–60 m/s	3% to 40 m/s 5% to 60 m/s
	Wind direction	0–359°	3° to 40 m/s 5° to 60 m/s
	Pressure	300–1100 hPa	5 hPa @ 25 °C
	Temperature	−40° C to +70 °C	0.3 °C @ 20 °C

where S_{ref} is the reference salinity (S = 33), $S_{(z)}$ is the salinity at a depth of $z = 20$ m, and D is the integration of the water column from the surface layer to the 20 m depth. The relationship between salinity and Kf is inverse, and when $Kf = 0$, the water column is fully mixed (Dávila et al., 2002).

Finally, we calculated PEA using the following equation:

$$PEA = \varphi = \frac{g}{h}\int_{-h}^{1}(\rho_m - \rho)zdz \quad (7)$$

where g is the acceleration due to gravity, h is the water column depth (20-m depth), ρ_m is the average surface water column density (1–20 m), and ρ is the density at depth z. When, $\phi = 0$, the water column is fully mixed, and when it is in the order of tens and hundreds, the classification applied is partially mixed and stratified, respectively.

3. Results

3.1. Annual cycles of hydrographic parameters and of the stability-mixing of the water column

The time series of surface conservative temperature (Θ) obtained hourly from the oceanographic buoy showed a clear annual cycle with warmer waters during austral spring–summer (16–18 °C) and colder waters during the austral winter (~10 °C; Fig. 2a). Within the annual surface cycle, less coherence was observed during the spring–summer transition among the different years (2018–2020) (Fig. 3a). The long-term monthly mean of surface Θ (Fig. 2b) revealed the warmest temperatures during February (Θ = 16.6 °C ± 1.01 °C) and the coldest in July (Θ of 10.25 ± 0.54 °C), closely following the mean annual cycle of air temperature (not shown). The monthly vertical profiles of Θ allowed the identification of water column warming during spring–summer (October–March) in approximately the first 20 m depth, although the less warming water reached ~50 m (Fig. 2c). In contrast, the lower layer (from 50 m to the bottom) warms from March to November (Θ range of 11.3–11.5 °C). Thus, the warming/cooling of the surface layer was out of phase with the cycle of the subsurface layer (Fig. 2c). The mean profile of Θ showed a high surface variability (0–20 m depth) with a standard deviation range of ±2.2– 3.1 °C (Fig. 2d). A stronger thermocline was identified in the profile that represented the average maximum vertical temperature (Fig. 2d, red line). In addition, a thermal inversion was visualized when the average of the vertical minimum temperatures was calculated (Fig. 2d, blue line).

The surface absolute salinity (S_A) time series from the buoy also exhibits an annual oscillation (15–31 g kg^{-1}), recording the lowest salinity from late winter (August) to the end of summer (March). High salinity of the surface water was observed during fall-winter, reaching a maximum S_A value of 32.64 g kg^{-1} on June 5, 2019 (Fig. 3a). The long-term monthly mean of surface S_A showed that during the winter months, salinity was on average high and stable (i.e., with low standard deviation) (Fig. 3b). The monthly profiles of S_A show a freshwater layer, whose influence extends down to ~15 m during spring-summer seasons (Fig. 3c).The subsurface salinity values oscillated during the year, as observed in the Θ profiles, recording the presence of Subantartic Water Mass (SAAW) and Modified Subantartic Water Mass (MSAAW) from

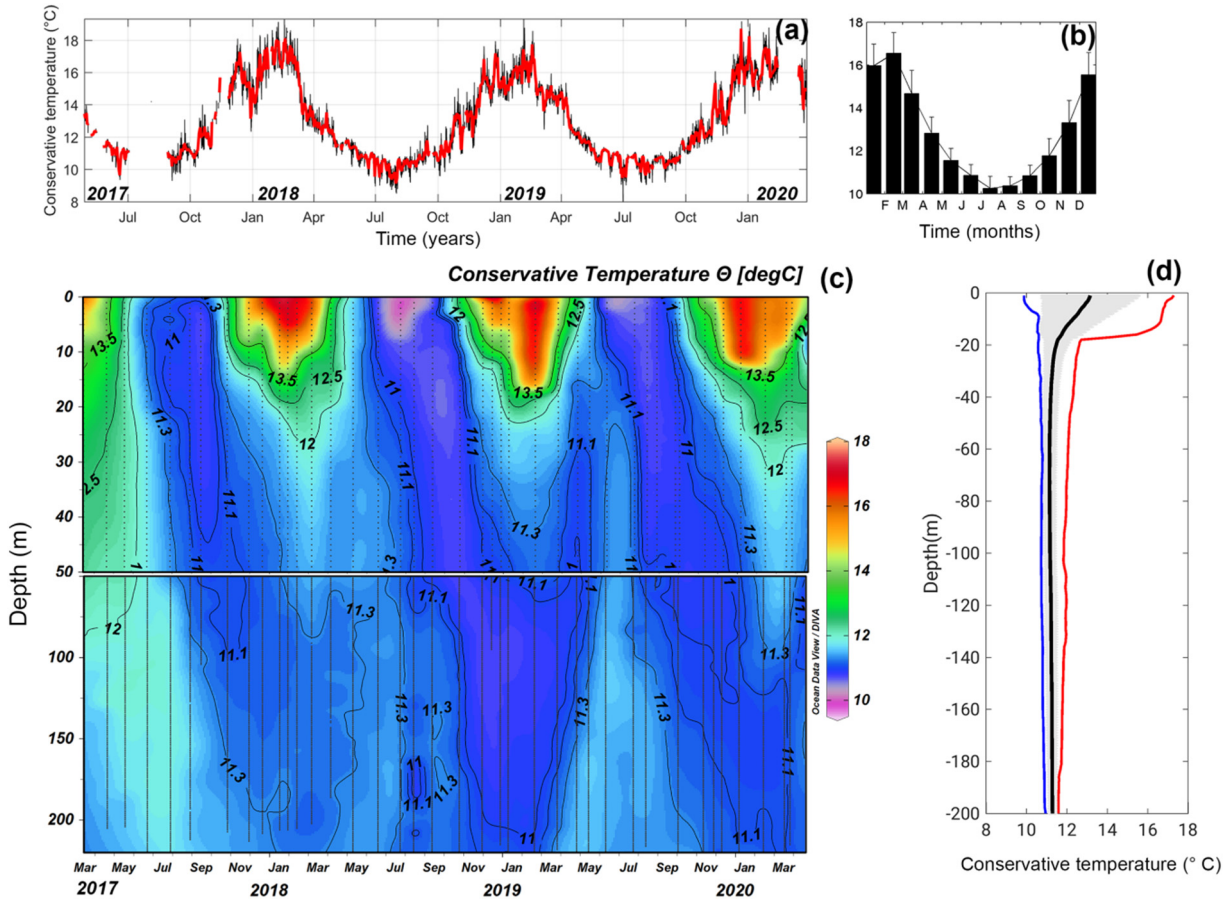

Fig. 2. Temporal distribution of conservative temperature from buoys (a), and long-term monthly means (black bar) with respective standard deviations shown as vertical bar (b). (c). Monthly time series, and (d) average (black line with standard deviation in shadow grey lines), maximum (red line), and minimum (blue line) profiles of conservative temperature obtained at the position of the oceanographic buoy. (For interpretation of the references to color in this figure legend, the reader is referred to the web version of this article.)

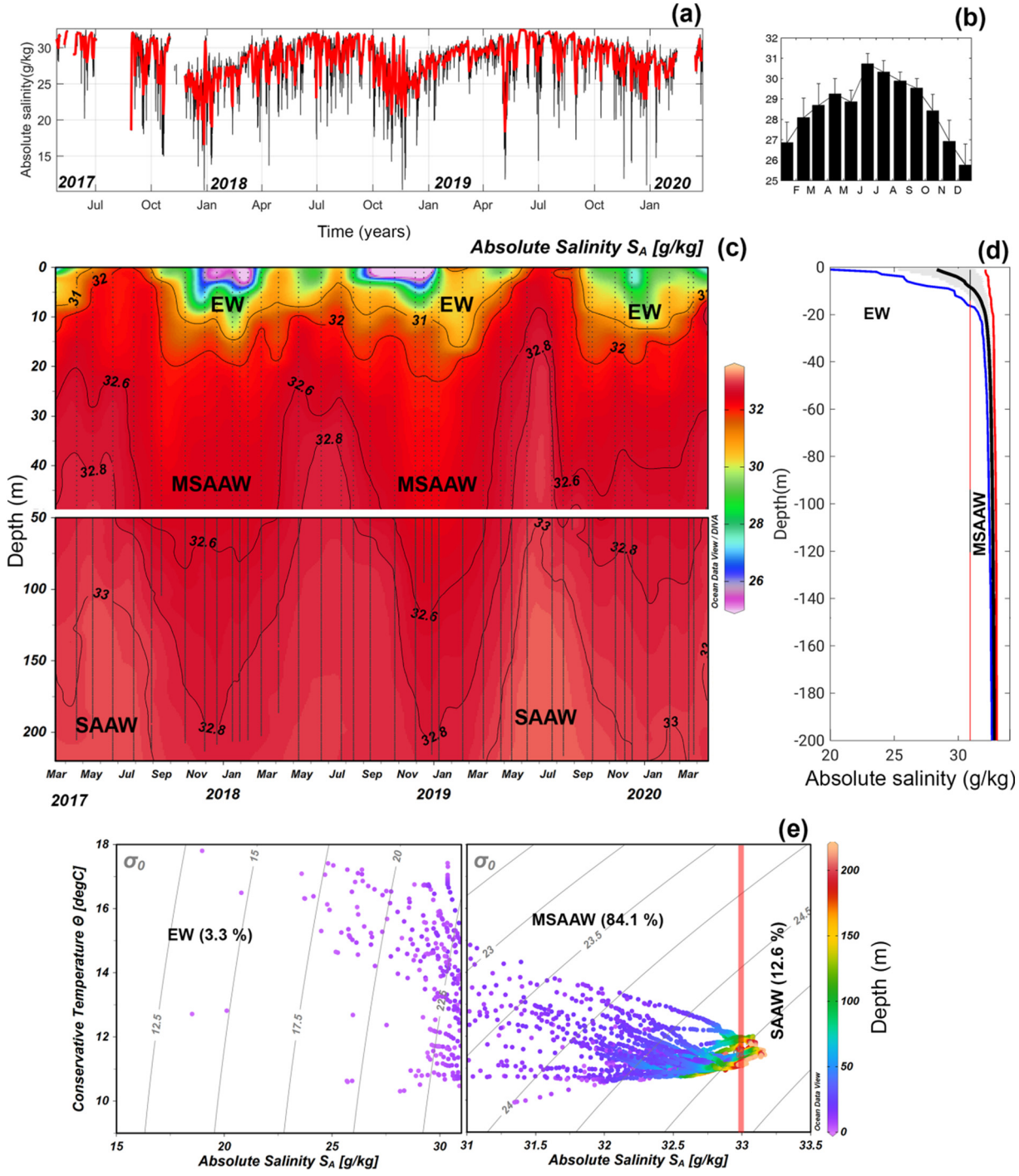

Fig. 3. Temporal and vertical variability of absolute salinity. (a) Temporal distribution of absolute salinity during the 3 year time series obtained at the position of the oceanographic buoy, (b) long-term monthly mean (black bar) and standard deviation (vertical bar) of the absolute salinity. (c) Monthly time series, and (d) average (black line with standard deviation in shadow grey lines), maximum (red line), and minimum (blue line) profiles of absolute salinity. (e) Water masses T-S diagram using data from the monthly time series. (For interpretation of the references to color in this figure legend, the reader is referred to the web version of this article.)

~15 m to the bottom (Fig. 3c). The S_A average profiles registered higher values and a standard deviation, denoting salinity fluctuations in the surface layer, where the EW (S_A 2–30 g kg^{-1}) was observed from 0 to 20 m (Fig. 3e). Below this layer, the standard deviation diminished, and the profile of the maximum salinities presented a homogeneous structure, representing the winter water column conditions (Fig. 3d). Finally, the water column (0–220 m) was dominated by the presence of the MSAAW with 84% of the records, followed by the SAWW with 13%, and EW with 3% (Fig. 3e).

3.2. Interannual cycles of the hydrographic and of the stability-mixing of the water column

Superimposed on their annual cycles, temperature, and salinity showed interannual variability in the 2017–2019 data record (Figs. 2 and 3). In the case of the vertical distribution of Θ, the water column reached the highest subsurface temperatures for the entire period from March to September 2017. For example, the 12 °C isotherm extended down to >70 m during May 2017, while it remained at about

30 m in other years. From November 2017 to March 2020, an asynchrony of warming was observed between the surface and subsurface layers, but this phenomenon was different every year. During March–September 2019,a relatively warm subsurface water reached ~20 m depth (Fig. 2c). At the same time, salty water reached the surface layer, as represented by the distribution of 32 g kg $^{-1}$ isohaline. A similar pattern was recorded during the fall-winter of 2017 (Fig. 3c). Moreover, the surface salinity values observed during the spring-summer of

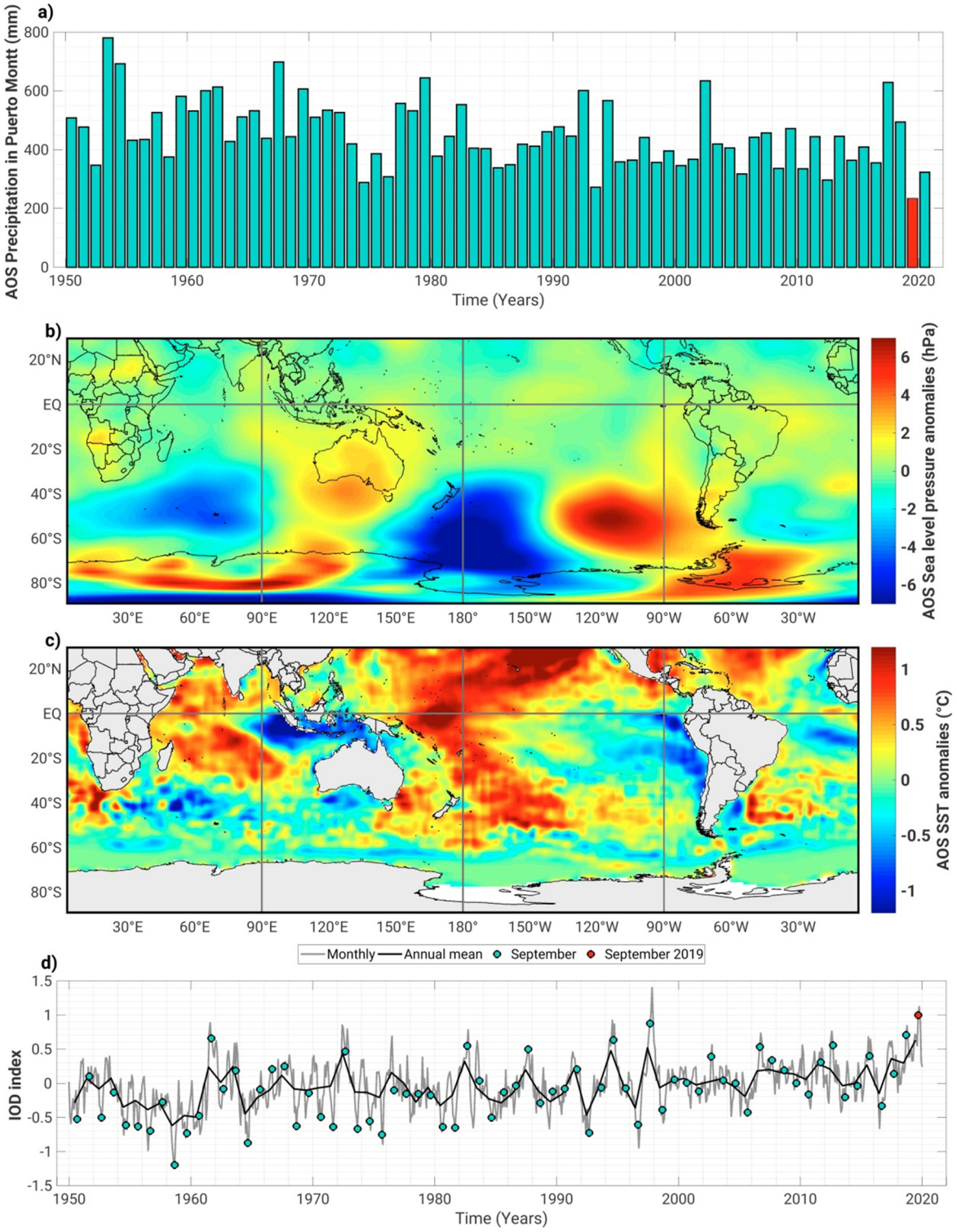

Fig. 4. Climate features of spring 2019. (a) August–September–October (AOS) accumulated precipitation at Puerto Montt (Tepual station DMC) from 1950 onwards. The record low AOS precipitation for 2019 is highlighted in red. (b) AOS sea level pressure anomalies (in hPa, scale at the left of the color bar) from NCEP-NCAR reanalysis. The grey arrow indicates a Rossby wave train across the South Pacific. (c) AOS sea surface temperature anomaly (in °C, scale at the right of the color bar) from the NOAA Optimal Interpolated SST (OISST-V3). The area that defines the Indian Ocean Dipole (IOD) is shown by the grey box. (d) Monthly values of the Indian Ocean Dipole index from the repository maintained by the NOAA Physical Sciences Laboratory (PSL) available online at https://www.psl.noaa.gov/data/climateindices. The IOD values during September are highlighted by the red circle. Note the record high IOD value in September 2019. (For interpretation of the references to color in this figure legend, the reader is referred to the web version of this article.)

2017–2018 and spring of 2018 were much lower than those during the spring-summer of 2019–2020.

In order to understand the interannual variability in surface salinity, and to elucidate the salinity maximum during the second half of 2019, precipitation data from Puerto Montt and river discharge from Puelo River were analyzed (Fig. S2). In general, precipitation is higher and more frequent during fall–winter (often in the range of 10–40 mm per day) and lower during spring–summer (with daily events of <10 mm). The long-term monthly mean and standard deviation values further reveal substantial year-to-year variability, especially during fall and early winter (Fig. S2). During our study period, dry conditions occurred in two years (2016 and 2019) but with different seasonality. Precipitation was extremely low during the summer and fall of 2016 with large, detrimental impacts on the environmental conditions of northern Patagonia. There was moderate precipitation deficit in the first half of 2019, but, in contrast to 2016, the dry conditions exacerbated from July to December, causing the driest spring in the last seven decades (Fig. 4a). Likewise, the Puelo River discharge reached its minimum value in September 2019 (Sup. Fig. S2). The pronounced seasonal drought in late winter and spring 2019 was associated with a broad area of intense, positive pressure anomalies (> + 5 hPa) located over the mid- to high latitudes of the southeast Pacific (Fig. 4b). Anticyclonic anomalies were also found in the middle and upper troposphere (not shown), reaching the west coast of South America, causing the weakening of the westerly flow to Patagonia, thus hindering the frontal system passage and precipitation that resulted in the regional precipitation deficit in later winter/spring 2019. The positioning of the positive and negative pressure anomalies over the South Pacific suggests a wave train emanating from Australia and arching eastward to reach southern South America (Fig. 4b). As discussed in Section 4, this wave train likely emerged in connection with intense SST and convection anomalies over the Indian Ocean (Fig. 4c), as reflected by the extremely high values that reached the Indian Ocean Dipole (IOD) index during August–September 2019 (Fig. 4d).

As freshwater contribution to Patagonian fjords impacts surface salinity directly, and therefore the water column stratification, the Brunt–Vaisala frequency (BV) was calculated using the monthly profiles of Θ and S_A (Fig. 5a). The BV maximum values covered the first 20 m depth with an absolute BV maximum (40–60 cycles h^{-1}) during the spring-summer season of 2018. In contrast, stability minima (10–20 cycles h^{-1}) occurred every fall-winter season (Fig. 5a). The different stratification indices and parameters used to quantify the importance of the freshwater input to the water column stability and mixing process indicated that the water column was never highly stratified (ns > 1). The time series of all parameters reported a weak stratification during the spring-summer of 2019–2020 (Fig. 5b).

3.3. Water column response to biogeochemical processes (annual cycle and interannual variability)

The hourly time series of surface DO show a maximum during the late winter-early spring, and a minimum during the fall-winter season (Fig. 6a). In addition, monthly vertical profiles of DO-saturation and the apparent oxygen utilization (AOU, not shown) offered the possibility observing the DO concentration distribution through the water column (Fig. 6b). The main features were: (a) the surface maximum DO saturation (9 mL L^{-1}–130%) and minimum AOU (−115 μmol kg^{-1}) extended until a depth of ~10 m during late winter September 2017 and September 2018; (b) the maximum DO (4–5 mL L^{-1}) and saturation (60–80%) extended deeper in the water column down to ~50 m depth from September–December every year, while during the period from September to December 2017, the water column was fully ventilated

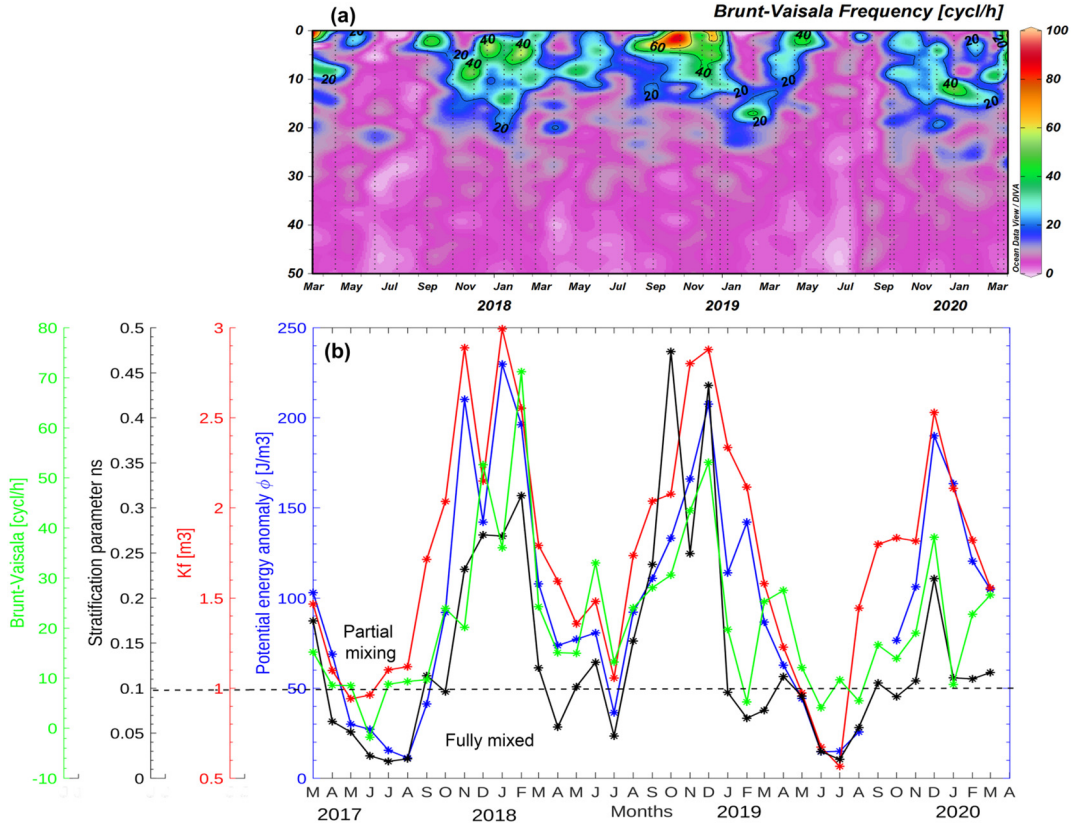

Fig. 5. Spatial and temporal variability of the water column stability indexes used in this study based on data obtained during the monthly sampling program at OMARE observatory. (a) Vertical distribution of Brünt-Vaisala frequency(N^2 in cycle*h^{-1}) (Stewart, 2002); (b) the time series variability of N^2 and other stability proxies as the stratification parameter (n_s) (Haralambidou et al., 2010) (black line), the surface brackish water layer (*Kf*) (red line) (Blanton and Atkinson, 1983), and the potential energy anomaly (PEA, ϕ) (Simpson et al., 1979) (blue line). (For interpretation of the references to color in this figure legend, the reader is referred to the web version of this article.)

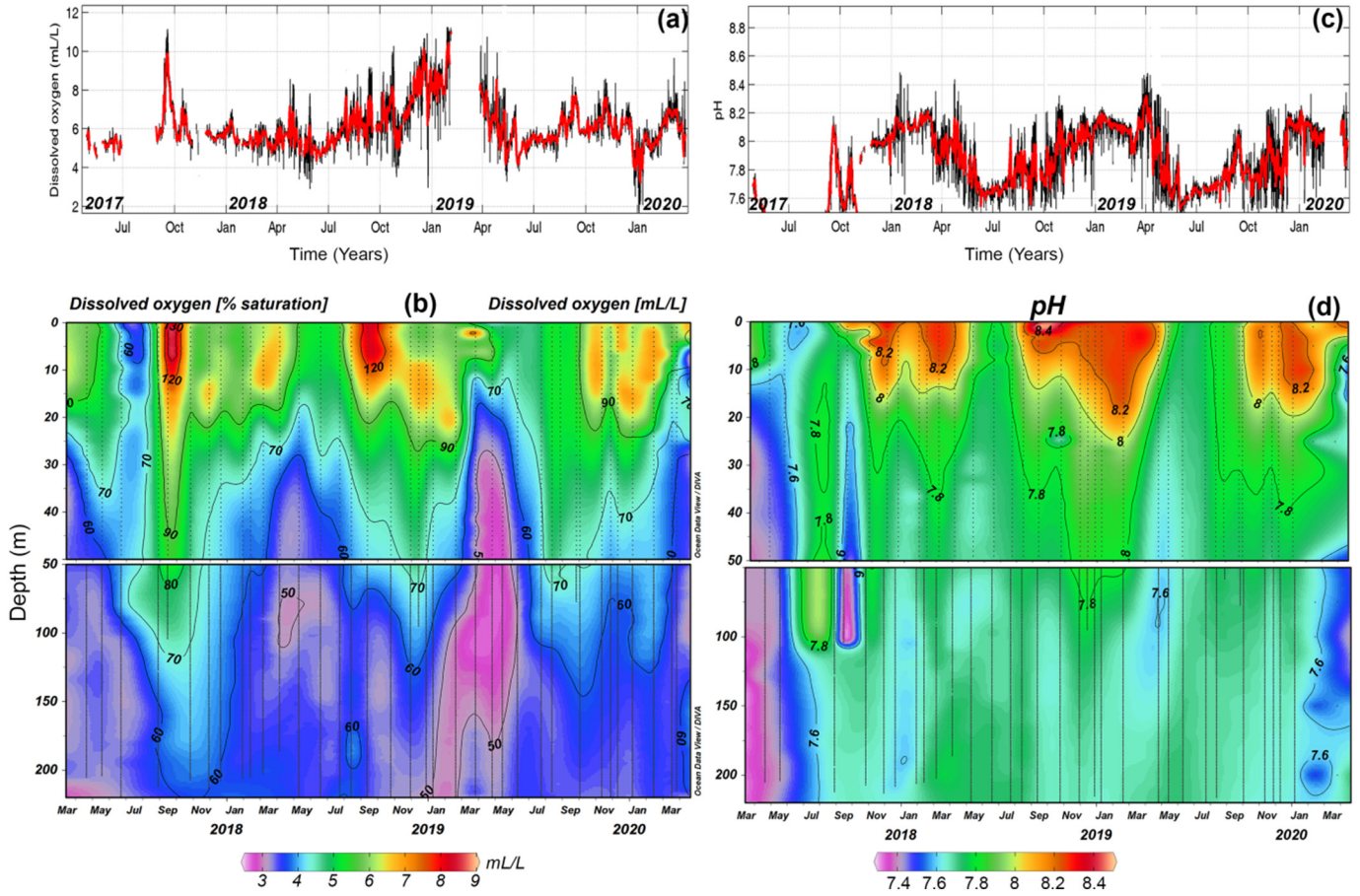

Fig. 6. (a, c) Temporal and (b, d) vertical variability of dissolved oxygen (mL L^{-1}) and pH during the 3-year study period based in the monthly time series program at the position of the oceanographic buoy in Reloncaví Sound.

with a saturation level of 60% near to 220 m depth; (c) the lowest DO-saturation and maximum AOU were observed from ~30 m to the bottom, from January–July. The DO (3 mL L^{-1}) and saturation (50%) were extremely low in 2019, but the AOU (140 μmol kg^{-1}) was higher and the maximum surface DO value during the late winter of 2019 was delayed when compared to the same period of 2017 and 2018.

The surface hourly pH time series showed a similar trend in the annual cycle as the DO, with maximum values occurring in spring-summer and partially in fall (pH = 8–8.2), and minimum values during winter (pH = 7.5–7.7), especially during June–July (Fig. 6c). The vertical profiles of pH revealed analogous patterns, as seen for DO, with a maximum in the pH in the upper 20 m, extending down to ~30–50 m from late winter to the summer every year (Fig. 6d). Overall, higher pH values correlate with higher DO concentrations, and vice versa ($R^2 = 0.45$, $n = 6822$).

The vertical time series of inorganic nutrients had a high spatial and seasonal variability distribution in the Reloncaví Sound. An annual trend for nitrate and phosphate was recorded at the surface layer (S < 31; EW), with an increase in both nutrients (Fig. 7a and c) during fall and early winter every year. The fall of 2019 was the period with the highest nitrate concentration at the surface layer (>25 μM). In contrast, the concentration of nitrate and phosphate was very low during summer. The highest concentration of phosphate in the surface water column occurred during winter 2019 (2.4 μM). Bellow the bottom layer, the annual cycle was not observed, and the concentration varied between 2.06and2.47 μM. In spring 2019, the concentration of phosphate below the bottom layer (100–150 m) was the highest of the entire study period (3.01 μM) (Fig. 7c). The concentration of NO_3 and PO_4 were highly correlated through the water column ($R^2 = 0.85$ $n = 390$). The nitrite concentration was low throughout the entire sampling period, with concentrations ranging between 0.1 and 0.4 μM. Finally, the corrected silicic acid concentration estimated (Si.SEF) showed the higher values at the surface layer during the spring of 2017 and summer of 2018 and 2019 (Fig. 7d). The highest average concentrations of corrected silicic acid were observed during the summer of 2018 (42 μM) and of 2019 (37 μM) between 100 and 150 m depth (Fig. 7d).

The N/P ratio showed a similar temporal and vertical pattern as nitrate and phosphate, with a minimum in the N/P ratio (0–6) found at the surface layer (S < 31; EW) during spring and summer. The maximum N/P (10−12) was observed in subsurface waters (Fig. 7e). The N/P ratio was lower than the Redfield ratio (16:1), with an average value of 9.08 ± 2.98. Historical N/P ratio records of the Reloncaví Sound obtained from 1995 to 2013 showed a similar trend ($R^2 = 0.92$, $n = 531$, and RMS = 2.49) with an average of 8.79 ± 3.6 (Sup. Fig. S3). In general, the N/P ratio from the OMARE time series and historical data was 99% under the Redfield ratio. Finally, the Si* was positive, with maximal values at surface waters (12–30 μM), and the absolute maximum recorded during spring of 2017 (Fig. 7f). In addition, positive Si* values (~4 μM) were observed in the subsurface layer (S > 31, MSAAW), specifically between 75 and 175 m depth, during the summer of 2018 and of the 2019. Negative Si* values were registered at a depth of 10 m, with an absolute minimum observed in the winter of 2019.

3.4. Phytoplankton distribution and density: case study of late winter and summer blooms

The vertical profiles of monthly sampled Chl-a allowed the determination of the phytoplankton distribution in the Reloncaví Sound (Fig. 8a). This time series was obtained by combining in situ Chl-*a* measurements and fluorescence records from the CTD-OF. The statistical

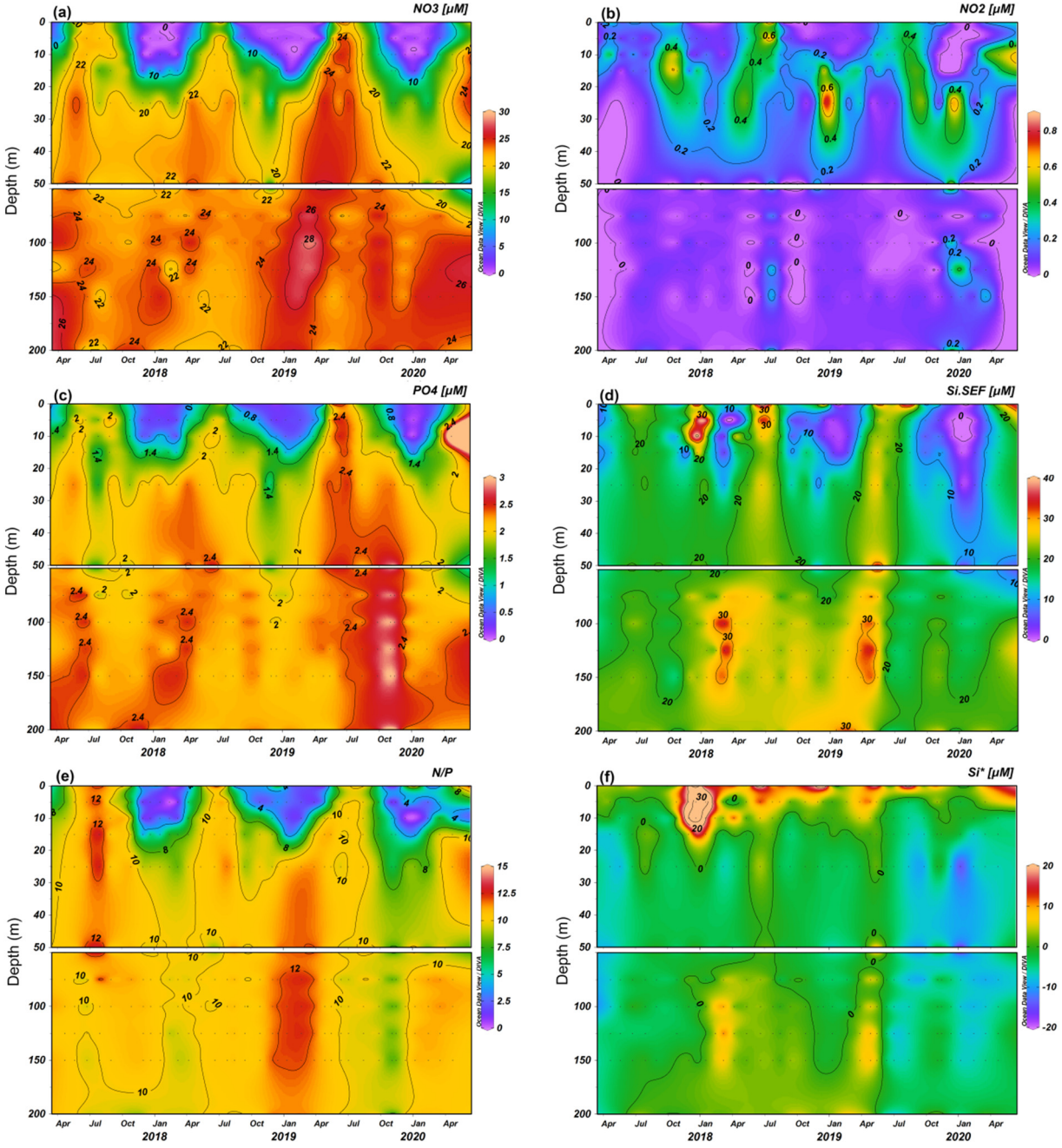

Fig. 7. Spatial and temporal distribution of inorganic dissolved nutrients: nitrate, nitrite, orthophosphate, and silicic acid corrected with salinity (NO_3^-, $NO2^-$, PO_4^{3-}, Si.SEF, respectively). Water samples were collected at the position of the oceanographic buoy during the 3 year monthly time series program. (a) NO_3^-, (b) NO_2^-, (c) PO_4^{3-}, (d) Si.SEF, (e) N/P, and (f) Si*.

correlation between both datasets was significant ($R^2 = 0.987$, $n = 222$). Overall, high Chl-*a* values were detected in the first 35 m depth, above the position of the pycnocline (isopycnal of 24 kg m^{-3}). Below this depth, the Chl-*a* concentrations were close to zero. The Chl-*a* increased during late winter (August–September), ranging from 10 to 35 μgL^{-1}, followed by a second and less intense maximum in summer, ranging from 10 to 15 μgL^{-1} (Fig. 8a). While the first peak was frequently observed at the surface (~5 m), the second peak was observed in subsurface waters (10–20 m). Minimum Chl-a values were measured during fall and early winter in 2018 and 2019 (no data for 2017during that season). The late winter bloom in 2019 was weak compared to the same period from 2017 to 2018. The causes of this decrease are discussed in Section 4.

In terms of phytoplankton composition, diatoms were the dominant taxonomic group within the phytoplankton community, followed by dinoflagellates (Fig. 8b). Diatoms reached relative abundance values >50% during the whole study period, while dinoflagellates were < 30%, except for May 2017 when *Heterocapsa triquetra* dominated (relative abundance of 64%). Six genera of diatoms were the most abundant during the study period: *Skeletonema*, *Pseudo-nitzschia*, *Rhizosolenia*, *Navicula*, *Chaetoceros,* and *Thalassiosira*. *Skeletonema* spp., *Pseudo-nitzschia* spp., *Rhizosolenia* spp., and *Navicula* spp. contributed up to 70% of the total phytoplankton relative abundance, while *Chaetoceros* spp. and *Thalassiosira* spp. were less abundant, but werehighly prevalent. The highest Chl-*a* concentrations (30–35 $\mu g\ L^{-1}$) were detected in September 2018 and January 2020 (Fig. 8a), when the phytoplankton community was characterized by a higher representation of *Skeletonema* spp. and *Pseudo-nitzschia* spp. In this context, a case study will be discussed below in order to explain the development of the microalgae bloom occurring from September 2018 to February 2019.

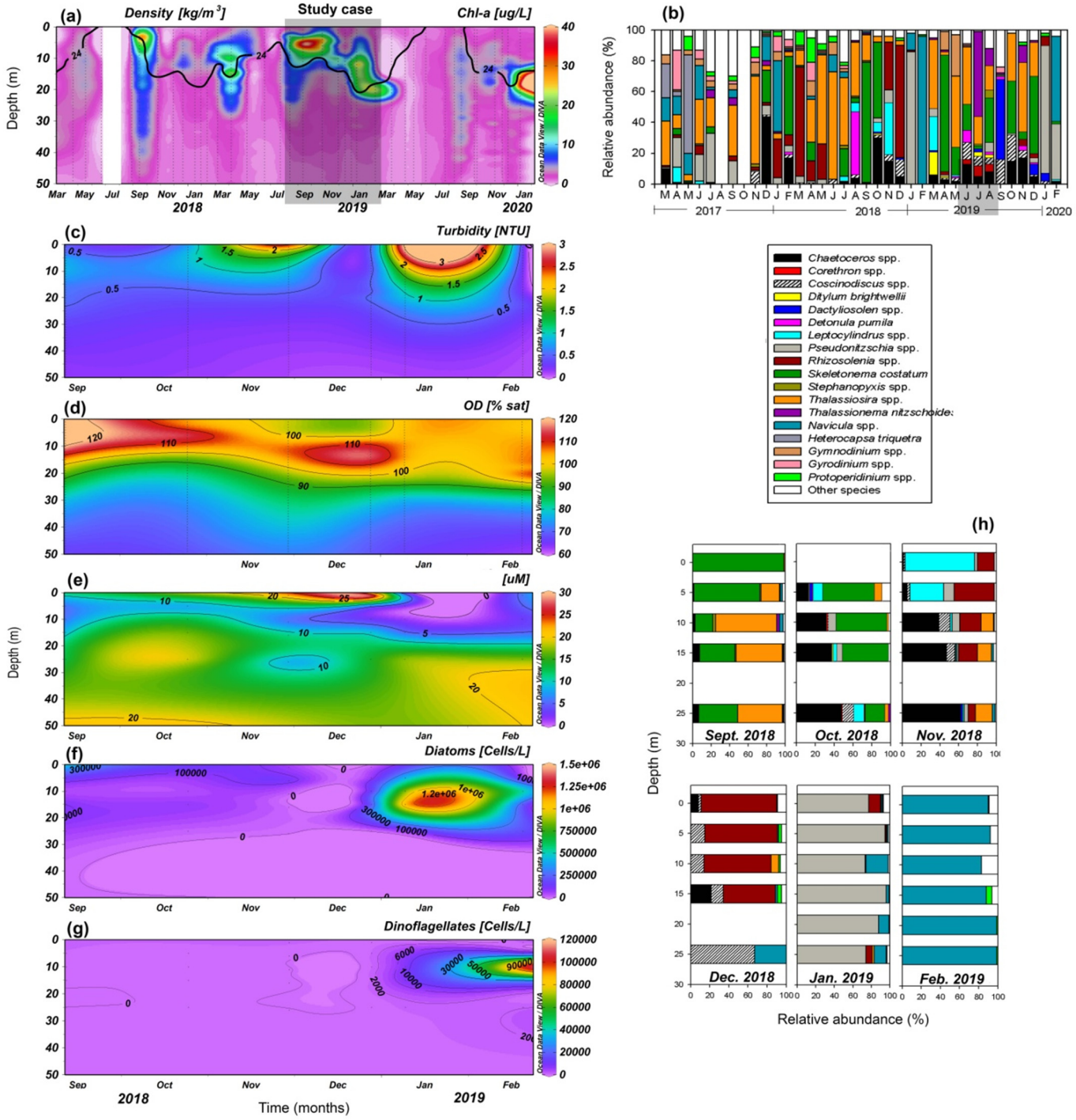

Fig. 8. (a) Vertical distribution patterns of Chlorophyll-*a* during the study period. (b) Relative abundance of phytoplankton species and (c–h), the evolution of physical, chemical, and phytoplankton assemblage's distribution during the study case of late winter 2018. The black line in (a) represented the isopycnal of 24 kg m^{-3}.

An intense surface Chl-a maxima (~40 μg L^{-1}) was observed in September 2018. This peak occurred at the base of the pycnocline, coinciding with the base of the turbidity and dissolved oxygen saturation maximum (Fig. 8c–d). This condition was sustained in October, but with lower levels of Chl-*a* (25 μg L^{-1}), until December (15 μg L^{-1}). In terms of community composition, in September 2018, a peak in diatoms density was observed at the surface, coinciding with the maximum PAR (150 uE sm^{-2}), and the lowest silicic acid concentration (Fig. 8e), this peak was dominated by *S. costatum* (Fig. 8f). A deepening in the Chl-*a* maxima was observed from September to December 2018 with a loosening of the peak sharpness, which was correlated with the lowest concentration of nutrients. A decrease diatoms density was also observed with a dominance of *Leptocylindrus* spp. in surface waters during November 2018, which turned to a dominance of *Rhizosolenia* spp. in December 2018 (Fig. 8f and g). During this month, an uncoupling between the Chl-*a* peak and DO saturation was observed, accompanied by a turbidity peak (~0.35 NTU) at 35 m depth below the pycnocline. The highest concentration of $Si(OH)_4$ (40 μM) at the surface layer (0–25 m depth) coincided with a lower density of diatoms and dinoflagellates at those depths. During January 2019, a second deeper, and intense Chl-*a* peak (25 μg L^{-1}) was observed at 15 m depth (a depth corresponding to 1% of the surface PAR) at the base of the pycnocline

and the DO saturation maxima. The maximum diatom density was quantified at this Chl-a peak, which was dominated by *Pseudonitzschia* spp. (Fig. 8h).In addition, a deepening of the Chl-*a* maxima occurred during February 2019,also peaking at the1% of the PAR, which was very high atthe surface layer (~1200 uE sm^{-2}). Here, the phytoplankton community was dominated by *Navicula* spp., with the highest dinoflagellates density (Fig. 8g and h), causing a complete depletion of nutrients at those depths.

4. Discussion

By analyzing the monthly time series and long-term records of the physicochemical and biological parameters in the Reloncaví fjord, we found a seasonal variation in the asynchrony input of oceanic and estuarine water. Estuarine water (warm and with lower salinity) arrives late winter to summer, followed by the irruption of higher salinity and colder oceanic water during fall-winter. The annual salinity variations in the photic layer and oceanic water mass contribute significantly to inorganic nutrient input. The N/P ratio values indicated that no eutrophication occurred when compared to historical data, even with the intense aquaculture activity occurring nowadays, likely due to the high ventilation dynamics of the Reloncaví Sound. The phytoplankton dynamics in the fjord are characterized by surface chlorophyll-a maxima in late winter and a deepening of spring–summer blooms related to the physicochemical conditions of the water column.

4.1. Surface layer processes

Historical measurements of the oceanography regime in Patagonian fjords detected a two-layer structure. The first layer is from the 0–15 m depth (S < 31; EW), and the second layer, from 15 m to the bottom (S > 31, MSAAW), depending on the fjords bathymetry (Castillo et al., 2016; Pérez-Santos et al., 2014; Pinilla et al., 2020a; Schneider et al., 2014; Sievers and Silva, 2008; Silva and Calvete, 2002; Valle-Levinson et al., 2007). These results were obtained during sporadic and/or seasonal oceanographic campaigns during the summer cruises of the CIMAR program. The OMARE observatory program opened a new opportunity to comprehend the long-term variability in the oceanography, and the biogeochemical conditions of the water column at a monthly resolution, which is largely dominated by the land-atmosphere-ocean interactions (Figs. 2 and 3).

The heating of the surface water (0–10 m depth) began in spring and extended until late summer, but considerable warming was observed down to ~50 m every year. This feature was already reported using a 3D hydrodynamic model of the Puyuhuapi fjord (Pinilla et al., 2020a). The input of continental fresh water is highest during late winter and early spring, contributing significantly to water column stratification (Fig. 5). The same pattern was previously reported for the study area (Schneider et al., 2014). Related to the onset of the water column stratification (late winter), there was an increase in DO and pH (Fig. 6) and a decrease in inorganic nutrients (e.g., NO_3^-, NO_2^-, $PO_4^{3-}$and $Si(OH)_4$, Fig. 7). These conditions are a response to enhanced primary production (PP) and carbon sequestration, both occurring at the photic layer.

In fact, recent studies have shown seasonal changes in the carbonate saturation states in sea–atmosphere fluxes of CO_2 in the same area (Vergara-Jara et al., 2019), and have concluded that the annual cycle of CO_2 fluxes was mainly governed by seasonal changes in biological processes that enhanced the shift from CO_2 sink in spring-summer to CO_2 source during the rest of the year. In the Patagonian fjords, the PP occurred in two stages: a long productive season from late winter to summer dominated by diatom blooms, and a shorter, non-productive season from fall to winter in which small phytoplankton cells prevailed (Montero et al., 2017a). However, transient events, such as the passage of frontal systems and mid-latitude cyclones, can also contribute to high levels of PP (Montero et al., 2017b) and increased carbon sequestration into the fjord during winter. The intense wind regime, high light conditions, continental freshwater discharge, the input of silicic acid, and water column stabilization appeared to act as the main factors triggering the PP process during the spring-summer seasons in Patagonian fjords (Iriarte and González, 2008; González et al., 2010; Montero et al., 2011; Iriarte et al., 2014; Jacob et al., 2014). In contrast, during fall-winter months, a combination of lower pH, as well as a decrease in DO and an increase in nutrients, could be attributed to multiple biogeochemical and physical processes: (a) the mixing of dissolved oxygen-poor deep water from below the halocline up to the surface layer (i.e., July 2017) followed the Reloncaví Fjord dynamics (Castillo et al., 2016; González et al., 2010; León-Muñoz et al., 2013); (b) enhanced post bloom heterotrophic processes, as was shown by Montero et al. (2011) and Olsen et al. (2014); and (c) allochthonous organic matter transported to the fjord that increases the water turbidity (data not shown) by runoff from heavy rain events during winter months (Rebolledo et al., 2015). Our results highlight the role of the freshwater input during the later winter in causing vertical stratification, and delivering of inorganic nutrients into the surface layer. These are important features that promote the use of nutrients by phytoplankton, triggering biological productivity in the following spring-summer season (Fig. 7). Primary production processes subside the availability of DO in these aquatic ecosystems, which is considered a good proxy of water quality indices (Zhang, 2019), and motivates their assessment for future research in Patagonian fjords.

4.2. Climate anomalies altering asynchrony during 2019 by Indian Ocean Dipole mode

The previous description broadly describes the mean annual cycles of physical and biogeochemical variables. Each year, however, has distinct climatic anomalies that can alter such cycles. For instance, the dry conditions during winter/spring 2019 led to a lower than average freshwater input and higher salinity in the upper layer (Fig. 3). This condition caused a decrease in the water column stability, as evidenced by the low Brünt-Vaisala frequencies (Fig. 5). The delayed, reduced freshwater supply was preceded by the intense advection of oceanic salty water in the winter of 2019. A rapid chemical response was observed, including a decrease in DO concentration and pH values, showing physical–chemical coupling in the Reloncaví Sound. In addition, a weak spring bloom with a low Chl-a concentration was also observed during this period in 2019, associated with high mixing in the water column and a drop in freshwater input. Freshwater inputs appear to stabilize the water column and increase the concentration of silicic acid, favoring the occurrence of diatom blooms (Montero et al., 2017a). In general, the phytoplankton community showed low densities during the winter months from June to August 2019, highlighting the presence of diatoms (e.g., *Corethron* spp. and *Thalassionema nitzschoides*), evidenced by the oceanic water advection in the study zone (Avarias et al., 2004). These phytoplankton species were observed only during the dry conditions during winter and spring 2019.

The case of spring 2019 adds to mounting evidence that anomalous biogeochemical conditions in the surface layer of the Patagonia fjord system are driven by regional precipitation anomalies (Díaz et al., 2021; Garreaud, 2018; León-Muñoz et al., 2018).The generally rainy conditions in Patagonia are strongly tied to the westerly winds over the Austral Andes, such that any disruption in the wind/pressure field results in precipitation anomalies. A tendency for drier than average summers under El Niño conditions has been previously reported (e.g., Montecinos and Aceituno, 2003). More recently, the positive phase of the SAM was associated with drought over Patagonia (Garreaud et al., 2008; Gillett et al., 2006). The long-term trend of the SAM towards positive polarity thus explains the drying that Patagonia has experienced in the last four decades (Boisier et al., 2019), and is projected to continue in the future (Aguayo et al., 2019). El Niño and the positive SAM phase acted in concert during summer and fall 2016 to produce the most severe drought on record with major

environmental impacts for Patagonia (Garreaud, 2018). Precipitation returned to its normal range for most of 2017 and 2018 (although February 2018 was also particularly dry at <50 mm; Díaz et al., 2021) but from summer 2019 onwards, it was below this range. Unlike the 2016 case, the rainfall deficit extended into the region's wet season (winter and spring) and caused the driest spring on record (Fig. 4a). The 2019 spring drought was unexpected because SAM was negative during most of the season and ENSO remained in its neutral phase, suggesting another mechanism impacted precipitation in western Patagonia. Following the work of Lim et al. (2021), we speculate that this mechanism was the Indian Ocean Dipole (IOD), the leading mode of year-to-year climate variability over the Indian Ocean, which is often maximized in austral spring (e.g., Saji et al., 1999). During August–September 2019, cold anomalies prevailed to the north of Australia, and warm anomalies over the tropical Indian Ocean (Fig. 4c) causing an extremely large IOD event, as shown by the time series of its index (Fig. 4d) and as analyzed in detail by Wang et al. (2020). The ensuing convection anomalies excited an atmospheric wave train (thick arrow in Fig. 4b) that sustained anticyclonic anomalies in the southeast Pacific, leading to a drought in northern Patagonia. The IOD has been linked to precipitation anomalies in tropical South America (Ashok et al., 2007; Chan et al., 2008) but this is the first time, to the best of our knowledge, that its remote effects are responsible for drought conditions in southern Chile.

4.3. Variability on phytoplankton assemblages during 2017–2019

Phytoplankton biomass in the ocean often shows strong vertical Chl-a concentration maxima arising from interactions with light, nutrient gradients (Ryan et al., 2010), and hydrodynamic gradients, such as stratification and vertical shear (Durham et al., 2009), which form a Chl-a maximum layer. This Chl-a maximum layer is also known as the thin phytoplankton layer (Durham and Stocker, 2012), where a large number of cells accumulate within a small depth range, typically from several centimeters to several meters thick (Dekshenieks et al., 2001). Subsurface Chl-a maxima usually occur in the water column as nutrients are depleted in the surface mixed layer (Huisman et al., 2006), and are widely found in the equator (e.g., Hopkinson and Barbeau, 2008) or towards the polar ocean (e.g., McLaughlin and Carmack, 2010). In stratified systems, Chl-a concentration peaks may form and persist for weeks to months. Indeed, in the Reloncaví fjord system, such peaks were periodically observed during spring and summer (Fig. 8a). However, they differ in the depths at which they occur and do not always coincide with the maximum density of diatoms and dinoflagellates (Fig. 8f and Fig. 8g). In this sense, dinoflagellates that often dominate in summer displayed the lowest chlorophyll content per biovolume. In general, chlorophyll content can fluctuate greatly throughout the year, depending on the light intensity, temperature, and phytoplankton composition (Felip and Catalan, 2000). The higher Chl-a values observed in late winter, rather than in summer, can be explained by both the lower light intensity reported in this period and by photo acclimation of the dominant species. Phytoplankton tends to increase the Chl-a content at reduced light intensities, while at higher radiances, such as that observed in summer, phytoplankton may enhance their cell numbers and decrease their Chl-a content (Beardall and Morris, 1976).

The spring-summer bloom in 2018–2019 allowed a better understanding of phytoplankton community dynamics in our study area (Fig. 8). First, due to the increase in the input of nutrients and light availability, an intense Chl-a peak occurred at the surface, which coincided with the maximum densities of diatoms and dinoflagellates. This peak lasted for three months, until December 2018. A taxa replacement was synchronic, and clearly observed with the deepening of the Chl-a peak starting with a dominance of *S. costatum,* characterized as a pioneer blooming species and ending with a dominance of *Rhizosolenia* spp. at lower densities than in the September 2018 bloom. The subsequent sinking of nutrient-stressed bloom cells may also result in a transient subsurface Chl-a maxima. This sinking was observed in the turbidity maxima that started in November 2018, with a maximum turbidity value (0.4 NTU) in December 2018. Phytoplankton experienced a trade-off between light (supplied by solar irradiance from the surface water column) and nutrients (supplied by upwelling and diffusion from depths below) (Mellard et al., 2011). In summer, as nutrients deplete from the surface waters, phytoplankton sink along with nutrients until light becomes the co-limiting factor (1% of surface PAR). These subsurface Chl-a maxima coincide with the nutricline and the dominance of *Pseudonitzschia* spp., which is a common genus in upwelling systems, also observed in subsurface Chl-a maxima in many different coastal locations globally (Trainer et al., 2012), and is recorded annually in Patagonian fjords, mainly during summer months (Montero et al., 2017a). The ability of some species of the *Pseudonitzschia* genera to grow under low light levels (Pan et al., 1996) explains the observed dominance of this group (>70%) at 20 m depth associated with a subsurface Chl-a maxima in the water column.

In the Patagonian fjords, one has to consider that the subsurface Chl-a peaks represent the abundance of a unique phytoplankton community, often differing substantially from that observed in the surface water column. In addition, the summer 2019 subsurface Chl-a maxima contribute to another autochthonous source of exported carbon to be considered as part of the biological pump. Understanding the mechanisms that drive phytoplankton community structure and variability in community succession is therefore crucial for the prediction of marine ecosystem fluctuations under changing environmental conditions, particularly in Fjords, where complex hydrodynamics and an intensive coupling between land and freshwater are likely to drive nutrient distribution and niche partitioning of phytoplankton communities (Margalef, 1978). Therefore, simulating the evolution of phytoplankton types in changing ocean scenarios is one of the main challenges in marine ecosystem modeling (Allen and Polimene, 2011; Finkel et al., 2010). In this sense, the OMARE program contributes to an interdisciplinary approach to study phytoplankton community succession in fjord ecosystems as a response to global and regional oceanography dynamics.

4.4. Subsurface layer processes

During the summer-fall of 2017, the water column was warm (Fig. 3), likely as a consequence of the coastal "El Niño" 2015/2016 event, being one of the strongest events reported since 1982 and 1997. However, the latter event registered extreme warm conditions, presumably due to anthropogenic forcing (Newman et al., 2018). In the adjacent oceanic area, as well as in the inner seas of the north Patagonian fjords, the sea surface temperature anomaly showed that warm conditions remained for the entire 2016– 2017 period (Narváez et al., 2019; Pérez-Santos et al., 2019). This explains the warmer conditions recorded in the water column of the Reloncaví Sound during the end of summer and winter of 2017. Here, SAAW, which originates at the surface layer in the open ocean in contact with the atmosphere (Silva et al., 2009), and was registered in the subsurface layer of Reloncaví Sound (Fig. 3), participated directly in the advection of the warm water registered during 2017. This water mass entered the north Patagonian fjord system mainly through the Guafo mouth into the Corcovado Gulf moving northward through the Ancud Gulf, Reloncaví Sound, and finally into the Reloncaví Fjord (Fig. 1b) (Pérez-Santos et al., 2014; Pérez-Santos, 2017; Sievers and Silva, 2008). However, more details on the physical mechanisms involved in the advection of warm water from the open ocean into the fjord system need to be investigated. In every fall–winter season from 2017 to 2019, oceanic water mass (SAAW) has advected from the subsurface layer in northern Patagonia, resulting in asynchrony of the water input to its fjord system (Figs. 2 and 3). Indeed, studies on the water age in Puyuhuapi fjord detected a significant statistical relationship between the circulation regimes and salinity fluctuations, for example, currents in the direction towards the inner fjord coincided with high salinity values and vice versa, supplying deep-water ventilation to help diminish the hypoxic conditions (Pinilla

et al., 2020a). Asynchrony of water ventilation between intermediate and deep water (Pinilla et al., 2020a) has been reported in other fjords around the world (e.g., Marinone and Pond, 1996; Pawlowicz, 2017). In northern Patagonia, the annual entry of subsurface warm salty oceanic water transports high inorganic nutrients (NO_3^-, PO_4^{3-}, and Si $(OH)_4$), and DO, sustaining high levels of primary production (Aracena et al., 2011; Montero et al., 2011; Daneri et al., 2012; Yevenes et al., 2017; González et al., 2019) and a high concentration of DO in the surface water column(9–10 mL L^{-1}, and100–130% of saturation, Fig. 6).

4.5. Explaining the asynchrony mechanism of oceanic water input

The hydrographic variability of intermediate and deep waters in the Reloncaví Sound strongly depends on the exchange with the ocean, specifically that which occurs at the bathymetric threshold of the Desertores pass (Fig. 1b), which restricts the passage of high-density deep-water masses (Ruiz et al., 2021; Salinas and Castillo, 2012; Silva and Vargas, 2014; Strub et al., 2019). Pinilla et al. (2020b), using a hydrodynamic model, reported that the renewal of deep waters from the Corcovado Gulf to the northern basin of the Desertores pass occurs from spring to autumn (Sup. Fig. S4), at which time the two-layer estuarine circulation is strengthened due to a greater stratification of the water column, allowing an increase in the intensity of the current towards the north in the deep layer (Sup. Fig. S5). In such a way, more saline water enters through this passage renewing the basins north of Desertores pass; these waters of higher density arrive in winter at the Reloncaví Sound, as shown by the observations in the OMARE buoy and the model (Fig. S6).

Hydrographic data from CIMAR cruises (Carrasco and Silva, 2005, 2006, 2007), as well as the results of the hydrodynamic model presented by Pinilla et al. (2020b) showed that the entry of deep ocean waters into the Corcovado Gulf is dominated by the presence of SAAW, which is saltier and colder than water masses (MSAAW, and EW) located in the northern most basins of the inner sea of Chiloé. This oceanographic context is produced by the intense mixing that occurs in the Desertores pass (Ruiz et al., 2021), contributing to the seasonal asynchrony between these water masses, as has been reported in this manuscript (Figs. 3 and 4). The simulations suggest that intense vertical mixing in the Desertores pass could be transported back towards the north through the subsurface layers, a part of the surface waters heated during the summer, which could be one of the explanations for the high temperatures recorded in Reloncaví Sound during winter.

A threshold similar to the Desertores pass in northern Patagonia is the Haro Strait in the Salish Sea, which is located in the fjord system of British Columbia in Canada. Here, mixing can be very intense, and some of this mixed water flows across the surface to the open ocean, and the other is transported into the Strait of Georgia through subsurface layers (Thomson, 1981; Pawlowicz, 2017). During late summer and early fall, warm, dense pulses of water descend into the deep basin of the Strait of Georgia (LeBlond et al., 1991; Masson, 2002). This warm signal can be explained by the strong mixing with warm surface water in the Haro Strait, resulting in relatively warm waters that subsequently advected to the Strait of Georgia during renewal pulses (LeBlond et al., 1991). During late winter and early spring, cold water with little change in salinity enters the deep basin of the Strait of Georgia as a result of mixing between the incoming Pacific Ocean waters and outgoing surface waters (Pawlowicz et al., 2017). We suggest that this mechanism of water renewal and transport observed in the fjord system in Canada is similar to that of the northern Patagonia.

4.6. Biogeochemical changes in Reloncaví sound using OMARE time series data

The availability of N and P in aquatic environments can affect the trophic food webs and biogeochemical cycles of carbon and nitrogen (Yan et al., 2016). Moreover, in these ecosystems, the N/P ratio can vary because of the differences in environmental factors and biological processes in the surface water column (Sereda and Hudson, 2011). The comparison between the N/P ratios from the OMARE time series with the historical measurements of N/P ratios (Sup. Fig. S3) showed similar results, suggesting that eutrophication processes were absent in our study area. The nutrient concentration in the adjacent oceanic water (Sup. Fig. S1) and the study area (Sup. Fig. S3) also demonstrated similarity with the nutrient time series obtained by the OMARE program in the Reloncaví Sound (Fig. 7). Nevertheless, high concentration of nutrients registered in the subsurface layer needs more investigations concerning the efficiency of remineralization processes occurring at the interior of the fjord. Finally, our results suggest that possible eutrophication due to aquaculture impact would only occur locally around farming cages. This research evidences the ecosystem services provided by local oceanography processes in the north Patagonian fjords. Here, the anthropogenic impact caused by economic activities could be, in part, chemically reduced by the annual ventilation cycle mediated by the exchange of oceanic water masses into Patagonian fjords.

Our investigation in Reloncaví Sound offers a better understanding of the interactions between coastal oceanography processes, atmospheric circulation, and the biogeochemical cycle responses. The OMARE observatory allowed the construction of a continuous time series of three years that detected the timing of the entrance of estuarine and oceanic waters into the north Patagonian fjords. The results provided by the observatory highlight the annual cyclicity between freshwater entering during spring and summer seasons, and oceanic waters arriving during fall and winter, both generating the asynchrony described in this investigation. However, this asynchrony could be constrained by atmospheric modes, i.e. IOD, as described in 2019. This mode could be associated with future scenarios of climate change, which suggest a reduction of the freshwater drainage towards these fjords, limiting stratification, the use of nutrients by phytoplankton, and weakening of primary production. These peculiarities can have consequences as a change in the phytoplankton composition, as we observed during 2019 with species characterized as oceanic into the Reloncaví Sound.

5. Conclusion

The OMARE oceanographic time series obtained from the monthly sampling program (2017–2019) in Northern Patagonia at the Reloncaví Sound allows an understanding of the importance of water exchange between the adjacent Southeast Pacific Ocean and the estuarine water from the Patagonian fjord system. Our results show that asynchrony provides an annual ventilation cycle mediated by the exchange of oceanic water. The asynchrony input of oceanic and estuarine waters began with subsurface SAAW from early fall to spring, while the EW entered from the surface layer during late winter to summer. Salinity at the surface layer showed interannual variability because of a decreasing precipitation trend and reduced river discharge during the spring-summer of 2019–2020. During this period, the intense seasonal drought could respond to the positive phase of the IOD mode, which was recognized as a new element causing precipitation variability in Southern Chile, similar to the roles of ENSO and SAM. The chemical parameters at the surface layer were synchronic with the physical variables of the water column, especially salinity. Every year, the salinity at the surface layer decreased with the arrival of freshwater during August–September, triggering the stratification processes. At this time, the DO and pH increased, and the nutrient concentration depleted by phytoplankton consumption. The results of the phytoplankton time series revealed a shift in community composition modulated by an increase in nutrient content. This condition favored the origin of an intense surface Chl-a peak during late winters, dominated by diatoms and dinoflagellates, followed by a deepening of the Chl-a peak and taxa replacement, which coincided with the nutricline position during the summer seasons. An interannual change in phytoplankton composition was

observed in2019 because the IOD mode delayed the late winter phytoplankton bloom, and oceanic species were subsequently found. The event that occurred during 2019corresponds to a case study of a future climate change scenario, providing a basis for new research to improve the use of valuable time-series data, enabling a holistic analysis of water quality and ecosystem services in Patagonian fjords.

CRediT authorship contribution statement

Iván Pérez-Santos: Study design, collection and analysis of physical oceanographic data, and manuscript leader. **Patricio A. Díaz:** Conceptualization, collection, and analysis of phytoplankton data, and manuscript revision. **Nelson Silva:** Analysis of nutrient sampling and manuscript revision **René Garreaud:** Analysis of climate data, [a]tmospheric indices, and manuscript revision. **Paulina Montero:** Conceptualization, analysis of phytoplankton data, and manuscript revision. **Carlos Henríquez-Castillo:** Conceptualization, analysis of phytoplankton data, and manuscript revision. **Facundo Barrera:** Conceptualization, analysis of biogeochemical data, and manuscript revision **Pamela Linford:** Conceptualization and analysis of physical oceanographic data. **Constanza Amaya:** Analysis of physical oceanographic data. **Sergio Contreras:** Conceptualization, analysis of biogeochemical data, and manuscript revision. **Claudia Aracena:** Conceptualization and manuscript revision. **Elías Pinilla:** Hydrodynamical model design and manuscript revision. **Robinson Altamirano:** OMARE data collection. **Luis Vallejos:** OMARE data collection. **Javiera Pavez:** Phytoplankton analysis. **Juan Maulen:** Phytoplankton analysis. All the authors contributed to the writing of the manuscript.

Funding

This research was funded by the FONDEQUIP Grant EQM160167 Project and the ULAGOS/DIRECCION DE INVESTIGACION Grant CR255. Iván Pérez-Santos was also funded by COPAS Sur-Austral AFB170006 and CIEP R20F002. Facundo Barrera thanks FONDECYT 3180307.

Declaration of competing interest

The authors declare that they have no conflicts of interest.

Acknowledgments

We thank Paola Reinoso for her help in performing nutrient analysis at the chemical laboratory of Pontificia Universidad Católica de Valparaíso, Chile. In memoriam to Professor Nelson Silva, a pioneer of oceanographic research in the Patagonian fjord region. We grateful to FONDAP-COPAS Center for motivate the creation of oceanographic time series in Chile.

Appendix A. Supplementary data

Supplementary data to this article can be found online at https://doi.org/10.1016/j.scitotenv.2021.149241.

References

Aguayo, R., Leon, J., Vargas-Baecheler, J., Montecinos, A., Garreaud, R., Urbina, M., Soto, D., Iriarte, J., 2019. The glass half-empty: climate change drives lower freshwater input in the coastal system of the chilean northern Patagonia. Clim. Chang. https://doi.org/10.1007/s10584-019-02495-6.

Aitkenhead, J.A., McDowell, W.H., 2000. Soil C: N ratio as predictor of annual riverine DOC flux at local and global scales. Glob. Biogeochem. Cycles 14, 127–138.

Allen, J.I., Polimene, L., 2011. Linking physiology to ecology: towards a new generation of plankton models. J. Plankton Res. 33 (7), 989–997.

Andersen, J.H., Schlüter, L., Ærtebjerg, G., 2006. Coastal eutrophication: recent developments in definitions and implications for monitoring strategies. J. Plankton Res. 28, 621–628.

Aracena, C., 2005. Seismic stratigraphy and Late Quaternary geological history of Reloncaví system, North patagonian fjords region, Southern Chile. Master of Science in Advanced Studies in Marine and Lacustrine Sciences. Universiteit Gent.

Aracena, C., Lange, C.B., Luis Iriarte, J.L., Rebolledo, L., Pantoja, S., 2011. Latitudinal patterns of export production recorded in surface sediments of the Chilean patagonian fjords (41–55° S) as a response to water column productivity. Cont. Shelf Res. 31, 340–355.

Arjonilla, M., Blasco, J., 2003. Nutrient analysis in estuarine water. Effect of salinity. Cienc. Mar. 29 (4), 389–395.

Ashok, K., Nakamura, H., Yamagata, T., 2007. Impacts of ENSO and Indian Ocean dipole events on the southern hemisphere storm-track activity during austral winter. J. Clim. 20, 3147–3163. https://doi.org/10.1175/JCLI4155.1.

Atlas, E.S., Hager, S., Gordon, L., Park, P., 1971. A Practical Manual for Use of the Technicon Autoanalyser in Sea Water Nutrient Analyses. Department of Oceanography. Oregon State University, Corvallis, OR.

Avarias, S., Cáceres, C., Muñoz, P., 2004. Distribution of marine microphytoplankton between Golfo Corcovado and Estero Elefantes in spring 1998 and summer 1999. Cienc. Tecnol. 27, 17–47 Mar.

Beardall, J., Morris, I., 1976. The concept of light intensity adaptation in marine phytoplankton: some experiments with Phaeodactylum tricornutum. Mar. Biol. 37 (4), 377–387.

Becherer, J., Flöser, G., Umlauf, L., Burchard, H., 2016. Estuarine circulation versus tidal pumping: sediment transport in a well-mixed tidal inlet. J. Geophys. Res. Oceans 121, 6251–6270. https://doi.org/10.1002/2016JC011640.

Bianchi, T.S., Arndt, S., Austin, W.E.N., Benn, D.I., Bertrand, S., Cui, Xingqian, Faust, J.C., Koziorowska-Makuch, K., Moy, C.M., Savage, C., Smeaton, C., Smith, R.W., Syvitski, J., 2020. Fjords as aquatic critical zones (ACZs). (2020). Earth Sci. Rev. 203, 103145. https://doi.org/10.1016/j.earscirev.2020.103145 ISSN 0012-8252.

Blanton, J.O., Atkinson, L.P., 1983. Transport and fate of river discharge on the continental shelf of the south eastern United States. J. Geophys. Res. 88, 4730–4738.

Boisier, J.P., Alvarez-Garreton, C., Cordero, R., Damian, A., Gallardo, L., Garreaud, R., Lambert, F., Ramallo, C., Rojas, M., Rondanelli, R., 2019. Anthropogenic drying in Central-Southern Chile evidenced by long term observations and climate model simulations. Elem. Sci. Anth. 6, 74. https://doi.org/10.1525/elementa.328.

Boyer, Tim P., Garcia, Hernan E., Locarnini, Ricardo A., Zweng, Melissa M., Mishonov, Alexey V., Reagan, James R., Weathers, Katharine A., Baranova, Olga K., Seidov, Dan, Smolyar, Igor V., 2018. World Ocean Atlas 2018. NOAA National Centers for Environmental Information. Dataset. https://accession.nodc.noaa.gov/NCEI-WOA18.

Burchard, H., Hetland, R.D., Schulz, E., Schuttelaars, H.M., 2011. Drivers of residual estuarine circulation in tidally energetic estuaries: straight and irrotational channels with parabolic cross section. J. Phys. Oceanogr. 41, 548–570.

Burrell, D.C., 1988. Carbon flow in fjords. Oceanogr. Mar. Biol. Annu. Rev. 143–226.

Calvete, C., Sobarzo, M., 2011. Quantification of the surface brackish water layer and frontal zones in southern Chile an fjords between boca del guafo (43300S) and estero elefantes (46300S). Cont. Shelf Res. 3, 162–171.

Carrasco, C., Silva, N., 2005. Distribución de temperatura, salinidad, oxígeno disuelto y nutrientes entre Puerto Montt y Boca del Guafo (CIMAR 10 Fiordos). Inf. Preliminares Crucero Cimar 10 Fiordos, pp. 35–45.

Carrasco, C., Silva, N., 2006. Distribución de temperatura, salinidad, oxígeno disuelto y nutrientes entre Puerto Montt y Boca del Guafo (CIMAR 11 Fiordos). Inf. Preliminares Crucero Cimar 11 Fiordos, pp. 37–47.

Carrasco, C., Silva, N., 2007. Distribución de temperatura, salinidad, oxígeno disuelto y nutrientes entre Puerto Montt y Boca del Guafo (CIMAR 12 Fiordos). Inf. Preliminares Crucero Cimar 12 Fiordos, pp. 35–46.

Carstensen, J., Krause-Jensen, D., Markager, S., Timmermann, K., Windolf, J., 2013. Water clarity and eelgrass responses to nitrogen reductions in the eutrophic Skive Fjord, Denmark. Hydrobiologia 704, 293–309.

Castillo, M.I., Pizarro, O., Cifuentes, U., Ramirez, N., Djurfeldt, L., 2012. Subtidal dynamics in a deep fjord of southern Chile. Contin. Shelf Res. 49, 73–89.

Castillo, M.I., Cifuentes, U., Pizarro, O., Djurfeldt, L., Cáceres, M., 2016. Seasonal hydrography and surface outflow in a fjord with a deep sill: the Reloncaví fjord, Chile. Ocean Sci. 12, 533–544.

Chan, S., Swadhin, K., Yamagata, T., 2008. Indian Ocean dipole influence on south american rainfall. Geophys. Res. Lett. 35, L14S12. https://doi.org/10.1029/2008GL034204.

Daneri, G., Montero, P., Lizárraga, L., Torres, R., Iriarte, J.L., Jacob, B., González, H.E., Tapia, F.J., 2012. Primary productivity and heterotrophic activity in an enclosed marine area of Central Patagonia (Puyuhuapi Channel; 44S, 73W). Biogeosci. Discuss. 9, 5929–5968.

Dávila, P.M., Figueroa, D., Müller, E., 2002. Freshwater input into the coastal ocean and its relation with the salinity distribution off austral Chile (35–55° S). Cont. Shelf Res. 22, 521–534.

Dekshenieks, M.M., Donaghay, P.L., Sullivan, J.M., Rines, J.E., Osborn, T.R., Twardowski, M.S., 2001. Temporal and spatial occurrence of thin phytoplankton layers in relation to physical processes. Mar. Ecol. Prog. Ser. 223, 61–71.

Díaz, P.A., Peréz-Santos, I., Álvarez, G., Garreaud, R., Pinilla, E., Díaz, M., Sandoval, A., Araya, M., Rengel, J., Montero, P., Pizarro, G., López, L., Iriarte, L., Igor, G., Reguera, B., Álvarez, F., 2021. Multiscale physical background to an exceptional harmful algal bloom of Dinophysis acuta in a fjord system. Sci. Total Environ. 773, 145621. https://doi.org/10.1016/j.scitotenv.2021.145621.

Durham, W.M., Stocker, R., 2012. Thin phytoplankton layers: characteristics, mechanisms, and consequences. Annu. Rev. Mar. Sci. 4, 177–207.

Durham, W.M., Kessler, J.O., Stocker, R., 2009. Disruption of vertical motility by shear triggers formation of thin phytoplankton layers. Science 323 (5917), 1067–1070.

Emery, W.J., 2001. Water types and water masses. Encyclopedia of Ocean Science, pp. 1556–1567.

Farmer, D.M., Freeland, H.J., 1983. The physical oceanography of fjords. Prog. Oceanogr. 12, 147–219.

Felip, M., Catalan, J., 2000. The relationship between phytoplankton biovolume and chlorophyll in a deep oligotrophic lake: decoupling in their spatial and temporal maxima. J. Plankton Res. 22 (1), 91–105.
Finkel, Z.V., Beardall, J., Flynn, K.J., Quigg, A., Rees, T.A.V., Raven, J.A., 2010. Phytoplankton in a changing world: cell size and elemental stoichiometry. J. Plankton Res. 32 (1), 119–137.
Garreaud, R.D., 2009. The Andes climate and weather. Adv. Geosci. 7, 1–9.
Garreaud, R., 2018. Record-breaking climate anomalies lead to severe drought and environmental disruption in Western Patagonia in 2016. Clim. Res. 74, 217–229. https://doi.org/10.3354/cr01505.
Garreaud, R., Vuille, M., Compagnucci, R., Marengo, J., 2008. Present-day South American Climate. PALAEO3 Special Issue (LOTRED South America). 281, pp. 180–195. https://doi.org/10.1016/j.paleo.2007.10.032.
Gillett, N., Kell, T., Jones, P., 2006. Regional climate impacts of the southern annular mode. Geophys. Res. Lett. 33, L23704.
González, H.E., Calderón, M.J., Castro, L., Clement, A., Cuevas, L.A., Daneri, G., Iriarte, J., Lizárraga, L., Martínez, R., Menschel, E., Silva, N., Carrasco, C., Valenzuela, C., Vargas, C., Molinet, C., 2010. Primary production and plankton dynamics in the Reloncaví Fjord and the interior sea of Chiloé, Northern Patagonia, Chile. Mar. Ecol. Prog. Ser. 402, 13–30. https://doi.org/10.3354/meps08360.
González, H.E., Castro, L.R., Daneri, G., Iriarte, J.L., Silva, N., Tapia, F., Teca, E., Vargas, C.A., 2013. Land-ocean gradient in haline stratification and its effects on plankton dynamics and trophic carbon fluxes in chilean patagonian fjords (47°–50° S). Prog. Oceanogr. 119, 32–47. https://doi.org/10.1016/j.pocean.2013.06.003.
González, H., Nimptsch, J., Giesecke, R., Silva, N., 2019. Organic matter distribution, composition and its possible fate in the chilean north-patagonian estuarine system. Sci. Total Environ. 657, 1419–1431. https://doi.org/10.1016/j.scitotenv.2018.11.445.
Hansen, D.V., Rattray, M., 1965. Gravitational circulation in straits and estuaries. J. Mar. Res. 23, 104–122.
Haralambidou, K., Sylaios, G., Tsihrintzis, V.A., 2010. Salt-wedge propagation in a Mediterranean micro-tidal river mouth. Estuar. Coast. Shelf Sci. 90, 174–184.
Hernández-Vaca, F., Schneider, W., Garcés-Vargas, J., 2017. Contribution of ekman pumping to the changes in properties and volume of the eastern South Pacific intermediate water. Gayana 81 (2), 52–63.
Holm-Hansen, C.J., Lorenzen, R.W., Holmes, J.D.H., 1965. Strickland fluorometric determination of chlorophyll. J. Cons. Int. Explor. Mer 30, 3–15.
Hopkinson, B.M., Barbeau, K.A., 2008. Interactive influences of iron and light limitation on phytoplankton at subsurface chlorophyll maxima in the eastern North Pacific. Limnol. Oceanogr. 53 (4), 1303–1318.
Hormazábal, S., Shaffer, G., Silva, N., Navarro, E., 2006. The Perú-Chile undercurrent and the oxygen minimum zone variability off Central Chile. Gayana 70, 37–45.
Huisman, J., Thi, N.N.P., Karl, D.M., Sommeijer, B., 2006. Reduced mixing generates oscillations and chaos in the oceanic deep chlorophyll maximum. Nature 439 (7074), 322–325.
Inall, M.E., Gillibrand, P.A., 2010. The physics of mid-latitude fjords: A review. Geological Society, London, UK, Special. Publications. 344, pp. 17–33.
Ioc, S., IAPSO, 2010. The international thermodynamic equation of seawater -2010: calculation and use of thermodynamic properties. Intergovernmental Oceanographic Commission, Manuals and Guides. 56. UNESCO 1-196 pages.
IPCC, 2013. The physical science basis. Contribution of working group I to the fifth assessment report of the intergovernmental panel on climate change. In: Stocker, T.F., Plattner, G.-K., Tignor, M., Allen, S.K., Boschung, J., Nauels, A., Xia, Y., Bex, V., Midgley, P.M. (Eds.), 1535 Climate Change. Cambridge University Press, Cambridge.
IPCC, 2014. 2014: synthesis report. Contributions of working groups I, II and III to the fifth assessment report of the Intergovernmental Panel on Climate Change. In: Pachauri, R.K., Meyer, L.A. (Eds.), Climate Change. IPCC, Geneva, pp. 1–151.
Iriarte, J.L., 2018. Natural and human influences on marine processes in patagonian subantarctic coastal waters. Front. Mar. Sci. 5, 360. https://doi.org/10.3389/fmars.2018.00360.
Iriarte, J.L., González, H.E., 2008. Phytoplankton bloom ecology of the inner sea of Chiloé, Southern Chile. Nova Hedwig. Beih. 133, 67–79.
Iriarte, J.L., González, H.E., Nahuelhual, L., 2010. Patagonian fjord ecosystems in southern Chile as a highly vulnerable region: problems and needs. Ambio 39, 463–466.
Iriarte, J.L., Pantoja, S., Daneri, G., 2014. Oceanographic processes in chilean fjords of Patagonia: from small to large-scale studies. Prog. Oceanogr. 129, 1–7.
Jacob, B.G., Tapia, F.J., Daneri, G., Iriarte, J.L., Montero, P., Sobarzo, M., Quiñones, R.A., 2014. Springtime size-fractionated primary production across hydrographic and PAR-light gradients in chilean Patagonia (41–50° S). Prog. Oceanogr. 129, 75–84.
Kalnay, E., Kanamitsu, M., Kistler, R., Collins, W., Deaven, D., Gandin, L., Iredell, M., Saha, S., White, G., Woollen, J., 1996. The NCEP/NCAR 40-year reanalysis project. Bull. Am. Meteorol. Soc. 77, 437–471.
LeBlond, P.H., Ma, H., Doherty, F., Pond, S., 1991. Deep and intermediate water replacement in the strait of Georgia. Atmosphere-Ocean 29, 288–312.
León-Muñoz, J., Marcé, R., Iriarte, J.L., 2013. Influence of hydrological regime of an andean river on salinity, temperature and oxygen in a Patagonia fjord, Chile. N.Z.J. Mar. Freshw. Res. 47, 515–528. https://doi.org/10.1080/00288330.2013.802700.
León-Muñoz, L., Urbina, M., Garreaud, R., Iriarte, J.L., 2018. Hydroclimatic conditions trigger record harmful algal bloom in western Patagonia (summer 2016). Sci. Rep. 8, 1330. https://doi.org/10.1038/s41598-018-19461-4.
Leth, O., Shaffer, Gary, Osvaldo, U., 2004. Hydrography of the eastern South Pacific Ocean: results from the Sonne 102 cruise, May–June 1995. Deep-Sea Res. II 51, 2349–2369.
Lim, E.P., Hendon, H., Butler, A., Thompson, D.W., Lawrence, Z., Scaife, A., Shepherd, T., Polichtchouk, I., Nakamura, H., Kobayashi, C., Comer, R., Coy, L., Dowdy, A., Garreaud, R., Newman, P., Wang, G., 2021. The 2019 southern hemisphere stratospheric polar vortex weakening and its impacts. Bull. Am. Meteorol. Soc. https://doi.org/10.1175/BAMS-D-20-0112.1.
Margalef, R., 1978. Life-forms of phytoplankton as survival alternatives in an unstable environment. Oceanol. Acta 1, 493–509.
Marinone, S.G., Pond, S., 1996. A three-dimensional model of deep water renewal and its influence on residual currents in the central strait of Georgia, Canada. Estuar. Coast. Shelf Sci. 43, 183–204.
Masson, D., 2002. Deep water renewal in the strait of Georgia. Estuar. Coast. Shelf Sci. 54, 115–126.
McLaughlin, F.A., Carmack, E.C., 2010. Deepening of the nutricline and chlorophyll maximum in the Canada Basin interior, 2003–2009. Geophys. Res. Lett. 37 (24).
Mellard, J.P., Yoshiyama, K., Litchman, E., Klausmeier, C.A., 2011. The vertical distribution of phytoplankton in stratified water columns. J. Theor. Biol. 269, 16–30.
Montecinos, A., Aceituno, P., 2003. Seasonality of the ENSO-related rainfall variability in Central Chile and associated circulation anomalies. J. Clim. 16 (2), 281–296.
Montero, P., Daneri, G., González, H.E., Iriarte, J.L., Tapia, F.J., Lizárraga, L., Sanchez, N., Pizarro, O., 2011. Seasonal variability of primary production in a fjord ecosystem of the Chilean Patagonia: implications for the transfer of carbon within pelagic food webs. Cont. Shelf Res. 31, 202–215.
Montero, P.M., Daneri, G., Tapia, F.J., Iriarte, J.L., Crawford, D., 2017a. Diatom blooms and primary production in a channel ecosystem of Central Patagonia. LAJAR 45, 999–1016.
Montero, P., Pérez-Santos, I., Daneri, G., Gutiérrez, M., Igor, G., Seguel, R., Crawford, D., Duncan, P., 2017b. Winter dinoflagellate bloom drives high rates of primary production in a patagonian fjord ecosystem. Estuar. Coast. Shelf Sci. 199, 105–116.
Narváez, D.A., Vargas, C.A., Cuevas, L.A., García-Loyola, S.A., Lara, C., Segura, C., Tapia, F.J., Broitman, B.R., 2019. Dominant scales of subtidal variability in coastal hydrography of the northern chilean Patagonia. J. Mar. Syst. 193, 59–73. https://doi.org/10.1016/j.jmarsys.2018.12.008.
Nazarnia, H., Nazarnia, M., Sarmasti, H., Wills, O., 2020. A systematic review of civil and environmental infrastructures for coastal adaptation to sea level rise. Civil Eng. J. 6 (7), 1375–1399.
Neshyba, S.J., Smith, R.L., Barber, R.T., Mooers, Ch.N.K., 1989. Poleward flows along eastern ocean boundaries. Costal and Estuaries Studies. 34. Springer Verlag 0-371 pp.
Newman, M., Wittenberg, A.T., Cheng, L., Compo, G.P., Smith, C.A., 2018. The extreme 2015/16 El Niño in the context of historical climate variability and change. Bull. Am. Meteorol. Soc. 99, S16–S20. https://doi.org/10.1175/BAMS-D-17-0116.1.
Olsen, L.M., Hernández, K.L., van Ardelan, M., Iriarte, J.L., Sánchez, N., González, H.E., Tokle, N., Olsen, Y., 2014. Responses in the microbial food web to increased rates of nutrient supply in a southern chilean fjord: possible implications of cage aquaculture. Aquacult. Environ. Interact. 6, 11–27. https://doi.org/10.3354/aei00114.
Pan, Y., Rao, D.V.S., Mann, K.H., 1996. Acclimation to low light intensity in photosynthesis and growth of Pseudo-nitzschia multiseries hasle, a neurotoxigenic diatom. J. Plankton Res. 18 (8), 1427–1438. https://doi.org/10.1093/plankt/18.8.1427.
Pawlowicz, R., 2001. A tracer method for determining transport in two-layer systems, applied to the strait of Georgia/Haro strait/Juan de fuca strait estuarine system. Estuarine Coastal and Shelf Science 52, 491–503.
Pawlowicz, R., 2017. Seasonal cycles, hypoxia, and renewal in a Coastal Fjord (Barkley sound, British Columbia). Atmosphere-Ocean 55, 264–283.
Penven, P., Echevin, V., Pasapera, J., Colas, F., Tam, J., 2005. Average circulation, seasonal cycle, and mesoscale dynamics of the Peru current system: a modeling approach. J. Geophys. Res. 110, C10021. https://doi.org/10.1029/2005JC002945.
Pérez-Santos, I., 2017. Deep ventilation event during fall and winter 2015 in the Puyuhuapi Fjord (44.6°S). Lat. Am. J. Aquat. Res. 45 (1), 223–227. https://doi.org/10.3856/vol45-issue1-fulltext-25.
Pérez-Santos, I., Garcés-Vargas, J., Schneider, W., Ross, L., Parra, S., Valle-Levinson, A., 2014. Double-diffusive layering and mixing in patagonian fjords. Prog. Oceanogr. 129, 35–49. https://doi.org/10.1016/j.pocean.2014.03.012.
Pérez-Santos, I., Seguel, R., Schneider, W., Linford, P., Donoso, D., Navarro, E., Amaya-Cárcamo, C., Pinilla, E., Daneri, G., 2019. Synoptic-scale variability of surface winds and ocean response to atmospheric forcing in the eastern austral Pacific Ocean. Ocean Sci. 15, 1247–1266. https://doi.org/10.5194/os-15-1247-2019.
Pinilla, E., Castillo, M.I., Pérez-Santos, I., Venegas, O., Valle-Levinson, A., 2020a. Water age variability in a patagonian fjord. J. Mar. Syst. 210. http://www.ncbi.nlm.nih.gov/pubmed/103376.
Pinilla, E., Soto, P., Soto-Riquelme, C., Venegas, O., Salas, P., Cortés, J., 2020b. Final report. Determinación de las Escalas de Intercambio de Agua en Fiordos y Canales de la Región de los Lagos y Región de Aysén del General Carlos Ibáñez del Campo. (Accessed noviembre 2020). Available online:. http://biblioteca.ifop.cl.
Quiñones, R.A., Fuentes, M., Montes, R.M., Soto, D., León-Muñoz, J., 2019. Environmental issues in Chilean salmon farming: a review. Rev. Aquac. 11, 375–402. https://doi.org/10.1111/raq.12337.
Rebolledo, L., Lange, C.B., Bertrand, S., Muñoz, P., Salamanca, M., Lazo, P., Iriarte, J.L., Vargas, G., Pantoja, S., Dezileau, L., 2015. Late holocene precipitation variability recorded in the sediments of Reloncaví Fjord (41°S, 72°W), Chile. Quat. Res. 84, 21–36. https://doi.org/10.1016/j.yqres.2015.05.006.
Rignot, E., Rivera, A., Casassa, G., 2003. Contribution of the Patagonia icefields of South America to sea level rise. Science 434–437. https://doi.org/10.1126/science.1087393.
Ruiz, C., Artal, O., Pinilla, E., Sepúlveda, H.H., 2021. Stratification and mixing in the Chilean Inland Sea using an operational model. Ocean Modell. 158. https://doi.org/10.1016/j.ocemod.2020.101750. http://www.ncbi.nlm.nih.gov/pubmed/101750.
Ryan, J.P., McManus, M.A., Sullivan, J.M., 2010. Interacting physical, chemical and biological forcing of phytoplankton thin-layer variability in Monterey Bay, California. Cont. Shelf Res. 30 (1), 7–16.
Saji, N., Goswami, B., Vinayachandran, P., Yamagata, T., 1999. A dipole mode in the tropical Indian Ocean. Nature 401, 360–363. https://doi.org/10.1038/43854.

Saldías, G.S., Sobarzo, M., Quiñones, R., 2019. Freshwater structure and its seasonal variability off western Patagonia. Prog. Oceanogr. 174, 143–153. https://doi.org/10.1016/j.pocean.2018.10.014.
Salinas, S., Castillo, M., 2012. Caracterización de las Corrientes mareales y submareales en el Canal Desertores (42°42' S; 72°50'W). Cienc. Tecnol. Mar. 35, 7–20.
Sauter, T., 2020. Revisiting extreme precipitation amounts over southern South America and implications for the patagonian icefields. Hydrol. Earth Syst. Sci. 24, 2003–2016.
Schneider, W., Pérez-Santos, I., Ross, L., Bravo, L., Seguel, R., Hernández, F., 2014. On the hydrography of puyuhuapi channel, Chilean Patagonia. Prog. Oceanogr. 129, 8–18.
Sereda, J.M., Hudson, J.J., 2011. Empirical models for predicting the excretion of nutrients (N and P) by aquatic metazoans: taxonomic differences in rates and element ratios. Freshw. Biol. 56 (2), 250–263. https://doi.org/10.1111/j.1365-2427.2010.02491.x.
Sievers, H., Silva, N., 2008. (Valparaíso). Water Masses and Circulation in Austral Chilean Channels and Fjords, Progress in the Oceanographic Knowledge of Chilean Interior Waters, From Puerto Montt to Cape Horn. Comité Oceanográfico Nacional – Pontificia Universidad Católica de Valparaíso, pp. 53–58.
Silva, N., Calvete, C., 2002. Physical and chemical oceanographic features of southern Chilean inlets between Penas Gulf and Magellan Strait (CimarFiordo 2 cruise). Cienc. Tecnol. Mar 25 (1), 23–88.
Silva, N., Vargas, C.A., 2014. Hypoxia in chilean patagonian fjords. Prog. Oceanogr. 129, 62–74.
Silva, N., Rojas, N., Fedele, A., 2009. Water masses in the Humboldt current system: properties, distribution, and the nitrate deficit as a chemical water mass tracer for equatorial subsurface water off Chile. DeepSea Res. II 56, 1004–1020.
Simpson, J.H., Edelsten, D.J., Edwards, A., Morris, N.C.G., Tett, P.B., 1979. The Islay front: physical structure and phytoplankton distribution. Estuar. Coast. Mar. Sci. 9 713–IN1.
Stewart, R.H., 2002. Introduction to. Phys. Oceanogr. 1–350.
Strickland, J.D.H., Parsons, T.R., 1972. A practical hand book of seawater analysis. 167. Fish. Res. Board Can. Bull. (Second. Edition), 1-310 pp.
Strub, P.T., James, C., Montecino, V., Rutllant, J.A., Blanco, J.L., 2019. Ocean circulation along the southern Chile transition region (38°–46°S): mean, seasonal and interannual variability, with a focus on 2014–2016. Prog. Oceanogr. 172, 159–198. https://doi.org/10.1016/j.pocean.2019.01.004 ISSN 0079-6611.
Thomson, R.E., 1981. Oceanography of the British Columbia Coast. Départ. Ment Fish. Oceans Sidney BC, pp. 1–56.
Tomas, C.R., 1997. Identifying Marine Phytoplankton. Academic Press, pp. 1–835.
Torres, R., Silva, N., Reid, B., Frangopulos, M., 2014. Silicic acid enrichment of subantarctic surface water from continental inputs along the patagonian archipelago interior sea (41–56° S). Prog. Oceanogr. 129, 50–61.
Trainer, V.L., Bates, S.S., Lundholm, N., Thessen, A.E., Cochlan, W.P., Adams, N.G., Trick, Ch. G., 2012. Pseudo-nitzschia physiological ecology, phylogeny, toxicity, monitoring and impacts on ecosystem health. Harmful Algae 14, 271–300. https://doi.org/10.1016/j.hal.2011.10.025.
Utermöhl, H., 1958. Zur Vervollkommnung der quantitativen Phytoplankton-Methodik. Int. Ver. Theor. Angew. Limnol. (9), 1–39 Komitee für Limnologische Methoden.
Valenzuela, R.A., Garreaud, R.D., 2019. Extreme daily rainfall in central-southern Chile and its relationship with low-level horizontal water vapor fluxes. J. Hydrometeorol. 20 (9), 1829–1850.
Valle-Levinson, A., 2010. Contemporary Issues in Estuarine Physics. Cambridge University Press, UK, pp. 273–307.
Valle-Levinson, A., Sarkar, N., Sanay, R., Soto, D., León, J., 2007. Spatial structure of hydrography and flow in a Chilean fjord, estuario Reloncaví. Estuar. Coast 30, 113–126.
Valle-Levinson, A., Cáceres, M.A., Pizarro, O., 2014. Variations of tidally driven three-layer residual circulation in fjords. Ocean Dynam. 64, 459–469.
Vergara-Jara, M.J., DeGrandpre, M.D., Torres, R., Beatty, C.M., Cuevas, L.A., Alarcón, E., Iriarte, J.L., 2019. Seasonal changes in carbonate saturation state and air-sea CO2 fluxes during an annual cycle in a stratified-temperate fjord (Reloncaví Fjord, chilean Patagonia). J. Geophys. Res. Biogeosci. 124, 2851–2865. https://doi.org/10.1029/2019JG005028.
Viale, M., Garreaud, R., 2015. Orographic effects of the subtropical and extratropical Andes on upwind precipitating clouds. J. Geophys. Res. Atmos. 120. https://doi.org/10.1002/2014JD023014.
Viale, M., Valenzuela, R., Garreaud, R., Ralph, F., 2018. Impacts of atmospheric Rivers on precipitation in southern South America. J. Hydrometeor. 19, 1671–1686. https://doi.org/10.1175/JHM-D-18-0006.1.
Wang, G., Cai, W., Yang, K., Santoso, A., Yamagata, T., 2020. A unique feature of the 2019 extreme positive Indian Ocean dipole event. Geophys. Res. Lett. 47, e2020GL088615. https://doi.org/10.1029/2020GL088615.
Yan, Z.B., Han, W.X., Penuelas, J., Sardans, J., Elser, J.J., Du, E.Z., Reich, P.B., Fang, J.Y., 2016. Phosphorus accumulates faster than nitrogen globally in freshwater ecosystems under anthropogenic impacts. Ecol. Lett. 19 (10), 1237–1246. https://doi.org/10.1111/ele.12658.
Yevenes, M.A., Bello, E., Sanhueza-Guevara, S., Farías, L., 2017. Spatial distribution of nitrous oxide (N2O) in the reloncaví estuary–sound and adjacent sea (41°–43° S), Chilean Patagonia. Estuar. Coasts 40, 807–821. https://doi.org/10.1007/s12237-016-0184-z (2017).
Zhang, L., 2019. Big data, knowledge mapping for sustainable development: a water quality index case study. Emerg. Sci. J. 3 (4), 249–254.